






Article

Model Predictive Control Design and Hardware in the Loop Validation for an Electric Vehicle Powertrain Based on Induction Motors

Jokin Uralde , Oscar Barambones , Eneko Artetxe , Isidro Calvo  and Asier del Rio 

Department of Systems Engineering and Automatic Control, Faculty of Engineering of Vitoria-Gasteiz, University of the Basque Country (UPV/EHU), 01006 Vitoria-Gasteiz, Spain; eneko.artetxe@ehu.eus (E.A.); isidro.calvo@ehu.eus (I.C.); asier.delrio@ehu.eus (A.d.R.)

* Correspondence: jokin.uralde@ehu.eus (J.U.); oscar.barambones@ehu.eus (O.B.)

Abstract: Electric vehicles (EV) have gained importance in recent years due to environmental pollution and the future scarcity of fossil resources. They have been the subject of study for many years, where much work has focused on batteries and the electric motor (EM). There are several types of motors in the market but the most widely used are induction motors, especially squirrel cage motors. Induction motors have also been extensively studied and, nowadays, there are several control methods used—for example, those based on vector control, such as field-oriented control (FOC) and direct torque control (DTC). Further, at a higher level, such as the speed loop, several types of controllers, such as proportional integral (PI) and model predictive control (MPC), have been tested. This paper shows a comparison between a Continuous Control Set MPC (CCS-MPC) and a conventional PI controller within the FOC method, both in simulation and hardware in the loop (HIL) tests, to control the speed of an induction motor for an EV powered by lithium-ion batteries. The comparison is composed of experiments based on the speed and quality of response and the controllers' stability. The results are shown graphically and numerically analyzed using performance metrics such as the integral of the absolute error (IAE), where the MPC shows a 50% improvement over the PI in the speed tracking performance. The efficiency of the MPC in battery consumption is also demonstrated, with 5.07 min more driving time.

Keywords: electric vehicle; hardware in the loop; model predictive control; induction motor



Citation: Uralde, J.; Barambones, O.; Artetxe, E.; Calvo, I.; del Rio, A. Model Predictive Control Design and Hardware in the Loop Validation for an Electric Vehicle Powertrain Based on Induction Motors. *Electronics* **2023**, *12*, 4516. <https://doi.org/10.3390/electronics12214516>

Academic Editor: Carlos Andrés García-Vázquez

Received: 3 October 2023

Revised: 27 October 2023

Accepted: 31 October 2023

Published: 2 November 2023



Copyright: © 2023 by the authors. Licensee MDPI, Basel, Switzerland. This article is an open access article distributed under the terms and conditions of the Creative Commons Attribution (CC BY) license (<https://creativecommons.org/licenses/by/4.0/>).

1. Introduction

Due to increasing air pollution, fuel shortages and growing environmental and energy concerns, the focus on electrifying the automotive sector has significantly intensified over the last ten years. Because of the problems associated with electric vehicles (EV), such as the price, the size of the batteries or the energy efficiency, the vehicle's propulsion system has garnered significant interest, alongside its related power electronics and energy storage devices, such as batteries. It has been explored in several works, such as [1,2], where battery management systems have been proposed, or in [3,4], where charging and discharging processes have been optimized. Furthermore, one area that has grown significantly and has been studied in recent years is autonomous cars. For example, studies have been carried out on the fault diagnosis of an autonomous car [5] and the optimization of vehicle trajectories [6,7], which is of great importance in preserving EV batteries.

The propulsion system of an EV is naturally made up of electric motors, which have been extensively researched and have seen widespread use in many other sectors outside the automotive sector; in fact, electric motors (EM) in industrial applications consume between 30% and 40% of the generated electrical energy worldwide [8]. In the automotive industry, there are four main types of EMs: brushed DC motors (BDCM), permanent magnet synchronous motors (PMSM), switched reluctance motors (SPM) and induction

motors (IM) [9]. This variety of motors has led some researchers to compare them in order to observe the differences and to assess their applications, such as the authors of [10], who point out that the IM needs more current than SPM and PMSM to achieve the same rated power due to the lower power factor (PF), although it has a very good overload capability. The authors of [11], on the other hand, conclude that PMSM provides efficiency rates of up to 97%. At low speeds, however, this advantage is lost as the permanent magnet eddy current losses increase by 50 times, resulting in around 1000 W of power loss. IM performs best, with the highest efficiency of 96% at high speeds. However, it has the widest low-efficiency region at low speeds due to copper losses. Nevertheless, IM is still the most common type of EM used in the automotive industry due to its low cost, robustness, little maintenance and reliability [12]. It should be mentioned that among the two types of IMs, wound rotors and squirrel cage rotors, it is the latter that are more widely used in most applications due to their lower price and lower maintenance [13].

Moving on to the control of IMs, the simplest variable-speed drive used to date is a scalar-based controller known as constant Volts per Hertz (V/f). However, its practical application at low frequencies is problematic due to the influence of the stator resistance and the necessary rotor slip to produce torque [14]. Nevertheless, some researchers have sought to improve this control method, like the authors of [15], who achieved current control assisted by V/f control, achieving the elimination of current peaks at the starting phase. However, V/f control applications are characterized by a slow torque and speed response (typically around 50 Hz/s) and a lack of significant load torque perturbations [16]. Therefore, the vector-based controller field-oriented control (FOC), which allows one to control an IM like a separated DC motor, achieving high performance control of the AC drives, is the most common and mature method to control AC drives in industry [17,18]. In [19], the authors compared FOC with a simpler predictive torque control (PTC), achieving similar results with both methods, but if the total harmonic distortion of the stator currents is measured, FOC achieves superior outcomes to PTC.

On the other hand, there is another vector-based control method that is extensively researched alongside FOC, which is direct torque control (DTC) [20], proposed to replace the decoupling control with bang bang control, which works effectively with the on/off operation of semiconductor power devices used in inverters. Compared with conventional FOC, the DTC scheme presents features such as no current control loops, no coordinate transformation and no separated pulse width modulator (PWM) [21]. Thus, several studies have been conducted comparing the two, such as in [22], where the researchers concluded that DTC is more suitable for highly dynamic applications, although it shows higher current and torque ripples. Moreover, they note other disadvantages of DTC, like the difficulty to control the torque and flux at low speeds, the high noise level at low speeds or the lack of direct current control.

In the field of power electronics and drives, model predictive control (MPC) has now become an established control technique [19]. The two main groups of predictive control applied in drive applications are Finite Control Set MPC (FCS-MPC) and Continuous Control Set MPC (CCS-MPC). The CCS-MPC control strategy assumes the continuous nature of the converter, i.e., the switching states of the semiconductors are not taken into account within the control algorithm. Therefore, a continuous control signal is generated and a modulator is used to generate the switching states, which produces an output with a fixed frequency. FCS-MPC, on the other hand, takes into account the discrete nature of the converters to formulate a less complex algorithm, which does not require modulation [23], although it causes high ripples in torque and current waves. It is true that with an optimal modulation index for the optimal voltage vector, FCS may provide equivalent performance to CCS. Nonetheless, FCS entails a significantly higher computational burden [24]. The researchers of [25] compared FCS-MPC with a PI-PWM control scheme, proving that although the tuning of the MPC was easier, it gave an 80% higher average phase current ripple and up to 20% for flux/torque control. Other authors [26] have performed a comparison of CCS-MPC with a conventional PI in a simulation that resulted in the better robustness of the MPC

against a load disturbance. Some improvements in FCS-MPC have been achieved in [27,28], where partition optimization and a predictive strategy that reduced the common-mode voltage at the machine terminals were used, respectively. Others [29] have proposed an online virtual voltage vector synthesis strategy to solve the current error generated by FCS-MPC, verifying its effectiveness against ordinary FCS-MPC. Nevertheless, the researchers of [28] compared it with sinusoidal pulse width modulation (SPWM) and it could not achieve the low total harmonic distortion (THD) current and torque ripple values shown by the SPWM.

On the other hand, real-time digital simulators have been applied in a variety of industries, such as the electrical, mechatronic and automotive industries, and the most popular and highly demanded application is the hardware in the loop (HIL) testing of digital controllers for AC motor drives [30]. HIL involves the integration of virtual components and real systems to evaluate the efficacy of control mechanisms on a virtual plant prior to utilization on a physical plant [31]. This method is useful in the first steps to configure an optimal control scheme for the control of a real EV motor, without taking any risks or damaging any equipment, especially power electronics.

This work introduces a comparative study for the vector control drive of an IM of an EV based on the CCS-MPC and PI techniques, which have been applied to control the speed of the motor. An FOC control method has been chosen over DTC due to the disadvantages indicated before, which outweigh its simplicity. CCS-MPC has been chosen over FCS-MPC due to the better torque ripple and THD current results with a modulation system, even if it is a more complex control strategy. In the power system, SPWM has been used to control the three-phase IGBT inverter, since it is less complex to implement than SVM and has better quality than hysteresis control. The validation of the proposed system has been considered both in simulation and real time alongside a battery consumption experiment, focusing on the improvement when using an MPC over a PI in EVs.

The structure of this manuscript is as follows. Section 2 provides a description of the hardware employed (the control board) and an overview of IM and ion-lithium batteries. Section 3 provides the theoretical development of the control algorithms used, the performance metrics used for further calculations and the sinusoidal pulse width modulation technique. The results are shown in Section 4 regarding the implementations in terms of error, robustness and battery consumption. Major conclusions of the research performed are provided in Section 5.

2. Materials and Methods

2.1. Hardware in the Loop

Experiments were carried out using a HIL environment, where the model to be controlled was simulated on hardware different from that of the controller. In this case, a dSPACE DS1202 MicroLaBox, a real-time control platform specifically developed for mechatronics development that can produce analog and digital signals, was used for the simulation of the electric motor. The device is powered by a programmable FPGA with a dual-core processor, allowing for up to 2 GHz, 1 GB DRAM and 128 MB flash memory. It also supports Real-Time Interface (RTI), a platform for fast and automatic C code generation, which enables designers to focus solely on the SIMULINK interface.

For the control scheme implementation, a dSPACE DS1104 was used, another real-time controller board used for research and development, aimed at rapid control prototyping. It has several input/output interfaces with a real-time processor that is able to reach up to 250 MHz.

Regarding the software involved, SIMULINK v10.6 from Matlab was used for the creation of the block diagrams. Otherwise, dSPACE offers support for the use of ControlDesk. This particular tool proves invaluable in visualizing real-time-acquired data, as well as recording and fine-tuning parameters such as control signals. The acquired data were then processed and graphically edited using Matlab.

The resulting hardware–software workflow is shown in Figure 1.

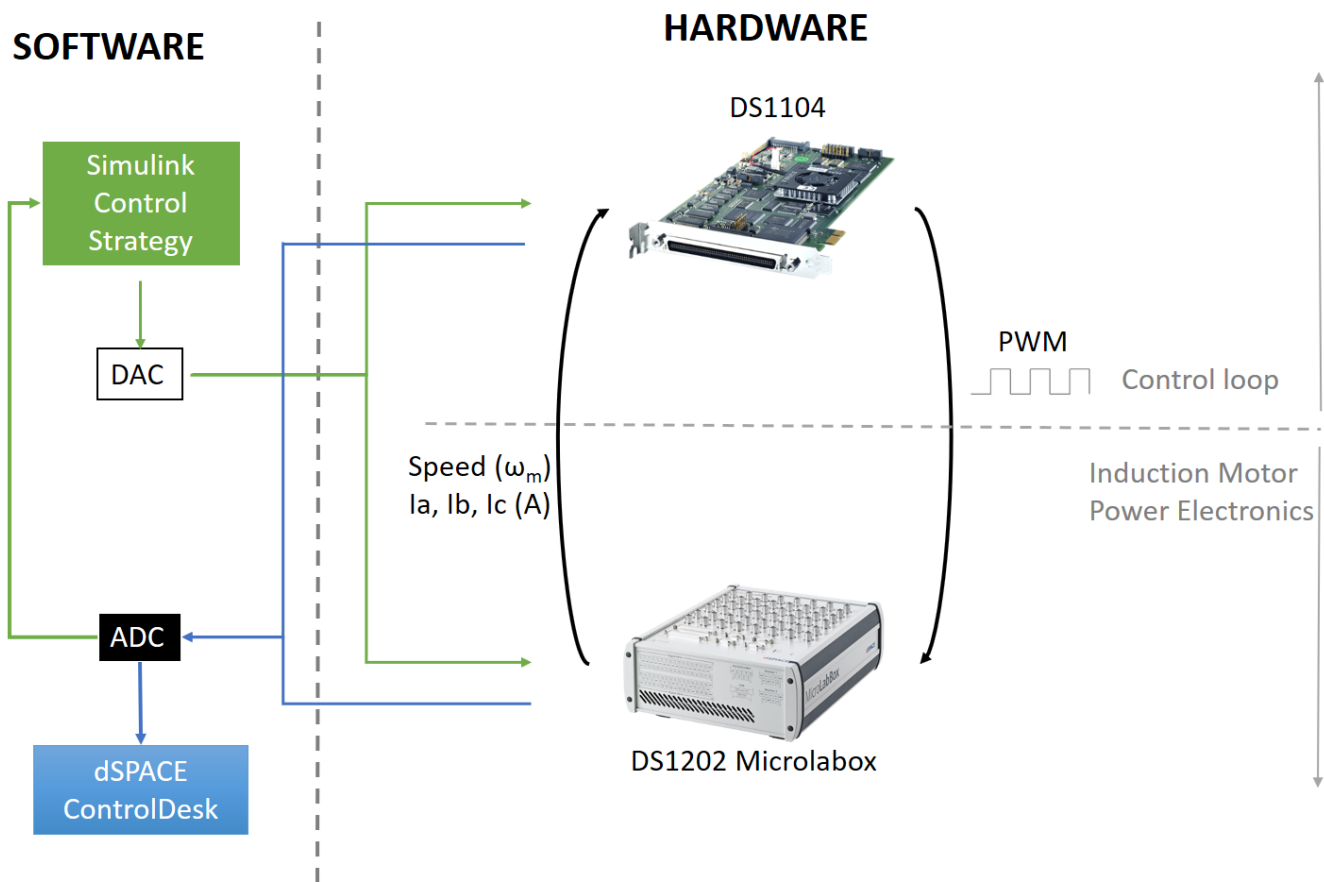


Figure 1. Hardware–software configuration designed for the HIL experiments.

It should be noted that the time step used for both dSPACE boards is limited by the computational load of the model or algorithm that they are running. The control algorithm should always be slower than the model to be controlled. Therefore, and because the Microlabox had a greater computing capacity, the DS1104 board executed the control algorithm at a sample rate of 1×10^{-4} s and the DS1202 board simulated the induction motor and the power electronics (inverter and batteries) at a sample rate of 5×10^{-5} s.

2.2. AC Induction Motors

Alternating current (AC) induction electric motors are widely used in electric vehicles due to their efficiency, reliability and ability to provide high starting torque. These motors consist of two main components: the stator and the rotor. The stator is the stationary part of the motor and is composed of wire coils arranged in pole structures. These coils are connected to an AC power source and generate a rotating magnetic field.

The rotor, on the other hand, is the rotating part of the motor. In induction motors, the rotor can be either a squirrel cage rotor or a wound rotor. In squirrel cage motors, the rotor consists of copper or aluminum rods short-circuited at both ends. When the rotating magnetic field from the stator cuts across the rotor, it induces a current in the rotor conductors. This creates a magnetic field in the rotor that interacts with the stator’s magnetic field, resulting in torque that drives the rotation of the motor.

An induction motor can be described through equations that couple the magnetic fluxes of each phase of the stator and rotor of the motor, which are shown in the following matrix in Equation (1).

$$\begin{bmatrix} \Psi_s \\ \Psi_r \end{bmatrix} = \begin{bmatrix} L_s & M_{sr} \\ M_{sr}^T & L_r \end{bmatrix} \begin{bmatrix} i_s \\ i_r \end{bmatrix} \quad (1)$$

$$\text{where } \Psi_s = \begin{bmatrix} \Psi_{sA} \\ \Psi_{sB} \\ \Psi_{sC} \end{bmatrix}, \Psi_r = \begin{bmatrix} \Psi_{ra} \\ \Psi_{rb} \\ \Psi_{rc} \end{bmatrix}, i_s = \begin{bmatrix} i_{sA} \\ i_{sB} \\ i_{sC} \end{bmatrix}, i_r = \begin{bmatrix} i_{ra} \\ i_{rb} \\ i_{rc} \end{bmatrix}, L_s = \begin{bmatrix} L_{sA} & L_{sAB} & L_{sAB} \\ L_{sAB} & L_{sA} & L_{sAB} \\ L_{sAB} & L_{sAB} & L_{sA} \end{bmatrix}, L_r = \begin{bmatrix} L_{ra} & L_{rab} & L_{rab} \\ L_{rab} & L_{ra} & L_{rab} \\ L_{rab} & L_{rab} & L_{ra} \end{bmatrix}, M_{sr} = \frac{N_r}{N_s} L_{sm} \begin{bmatrix} \cos\theta_r & \cos(\theta_r + 2\pi/3) & \cos(\theta_r - 2\pi/3) \\ \cos(\theta_r - 2\pi/3) & \cos\theta_r & \cos(\theta_r + 2\pi/3) \\ \cos(\theta_r + 2\pi/3) & \cos(\theta_r - 2\pi/3) & \cos\theta_r \end{bmatrix}.$$

By including equations that describe the ratios between the voltages in the motor windings and the coupling fluxes, the matrix model of natural three-phase coordinates is obtained, which relates the voltages of the windings to their respective currents based on the motor’s parameters (see Equation (2)).

$$\begin{bmatrix} v_s \\ v_r \end{bmatrix} = \begin{bmatrix} R_s & 0 \\ 0 & R_r \end{bmatrix} \begin{bmatrix} i_s \\ i_r \end{bmatrix} + s \begin{bmatrix} L_s & M_{sr} \\ M_{sr}^T & L_r \end{bmatrix} \begin{bmatrix} i_s \\ i_r \end{bmatrix} \tag{2}$$

being

$$v_s = \begin{bmatrix} v_{sA} \\ v_{sB} \\ v_{sC} \end{bmatrix}, v_r = \begin{bmatrix} v_{ra} \\ v_{rb} \\ v_{rc} \end{bmatrix}, R_s = \begin{bmatrix} R_s & 0 & 0 \\ 0 & R_s & 0 \\ 0 & 0 & R_s \end{bmatrix}, R_r = \begin{bmatrix} R_r & 0 & 0 \\ 0 & R_r & 0 \\ 0 & 0 & R_r \end{bmatrix}$$

where the variable *s* corresponds to the Laplace transform applied to the derivative function.

Furthermore, to finalize the motor modeling, it is essential to incorporate two equations involving the electromagnetic torque. The first equation shows the generation of electromagnetic torque by the motor and is defined as the cross product between the spatial vector of stator flux (*s*) and the spatial vector of rotor current (*r*) (Equation (3)). In this equation, *K_M* represents a parameter linked to the motor’s dimensions.

$$T_e = K_M \vec{\Psi}_r \times i_s \tag{3}$$

The second equation describes the mechanical dynamics of the motor, i.e., the balance of torque on its axis (Equation (4)).

$$J \frac{d\omega_m}{dt} + B_v \omega_m + T_L = T_e \tag{4}$$

where *J* is the inertia coefficient, *ω_m* is the mechanical speed, *B_v* is the friction coefficient, *T_L* is the torque of the load and *T_e* is the applied electromagnetic torque.

Model Used for Vector Control

First, it is necessary to explain the origin and the use of the components *d* and *q* of the rotating reference system, due to their relevance in the control algorithm.

In essence, an AC machine can be conceptualized as a transformer with a moving secondary component. As this secondary component moves, the coupling coefficients between the stationary stator and the rotating rotor phases undergo continuous alterations based on the rotor’s angular position, *θ_r*. The description of the machine’s behavior can be captured through a set of differential equations incorporating time-varying mutual inductances. However, employing such a model often leads to a notably intricate representation due to its inherent complexity [32]. Therefore, the simplification of the model is necessary for an optimal control.

We start with the three-phase current components A-B-C, and, by applying the Clarke transformation matrix, we obtain the two-phase components *α* and *β* of the stationary reference system (see Equation (5)). Similarly, the reverse operation can be performed

by using the inverse of the matrix from the preceding equation to derive the three-phase components from the two-phase components.

$$\begin{bmatrix} i_{s\alpha} \\ i_{s\beta} \end{bmatrix} = \begin{bmatrix} 1 & -\frac{1}{2} & -\frac{1}{2} \\ 0 & \frac{\sqrt{3}}{2} & -\frac{\sqrt{3}}{2} \end{bmatrix} \begin{bmatrix} i_{sA} \\ i_{sB} \\ i_{sC} \end{bmatrix} \tag{5}$$

It should be noted that the transformations between the three-phase A-B-C system and the two-phase α - β system, as described for the stator currents of the induction motor, can be perfectly applied to quantities such as stator voltages, currents, rotor currents and voltages and stator and rotor fluxes, among others.

As mentioned before, the motor model obtained by applying the Clarke transformation is defined in a stationary α - β two-phase reference system. However, the components of the spatial vector, such as \vec{i}_s , continue to be variables due to the relative angular displacement of the vector ω_e with respect to the stationary reference system. In order to prevent this, it is necessary to ensure that a d-q reference system moves at the same speed as the vector. In this way, the components of the vector \vec{i}_s in this new rotating d-q reference system remain constant.

Park transformation is the matrix, seen in Equation (6), used to transform the coordinates in the stationary two-phase system α - β of a vector into the coordinates of the rotating two-phase system d-q.

$$\begin{bmatrix} i_{sd} \\ i_{sq} \end{bmatrix} = \begin{bmatrix} \cos\theta_e & \sin\theta_e \\ -\sin\theta_e & \cos\theta_e \end{bmatrix} \begin{bmatrix} i_{s\alpha} \\ i_{s\beta} \end{bmatrix} \tag{6}$$

However, since the reference system in which the control algorithms operate is the rotating d-q two-phase system, it is common to use the matrix in Equation (7) to transition from the stationary A-B-C three-phase system to the d-q rotating system. This is done in order to enhance the utilization of machine models in control algorithms.

$$\begin{bmatrix} i_{sd} \\ i_{sq} \end{bmatrix} = \begin{bmatrix} \cos\theta_e & \cos(\theta_e - 2\pi/3) & \cos(\theta_e + 2\pi/3) \\ -\sin\theta_e & -\sin(\theta_e - 2\pi/3) & \sin(\theta_e + 2\pi/3) \end{bmatrix} \begin{bmatrix} i_{sA} \\ i_{sB} \\ i_{sC} \end{bmatrix} \tag{7}$$

where it is also common to use complex notation to express these transformations (the subscript r indicates rotating), as shown in Equation (8).

$$\vec{i}_{sr} = i_{sd} + ji_{sq} \tag{8}$$

After applying the transformations, the motor model in the new rotating d-q reference system is described by projecting the equations of this machine onto it. Thus, the stator and rotor equations can be described as the following Equations (9) and (10).

$$\vec{v}_{sr} = R_s \vec{i}_{sr} + \frac{d\vec{\Psi}_{sr}}{dt} + j\omega_e \vec{\Psi}_{sr} \tag{9}$$

$$\vec{v}_{rr} = R_r \vec{i}_{rr} + \frac{d\vec{\Psi}_{rr}}{dt} + j(\omega_e - \omega_r) \vec{\Psi}_{rr} \tag{10}$$

where R_s and R_r are the stator and rotor resistance, respectively; $\vec{\Psi}_s$ and $\vec{\Psi}_r$ are the stator and rotor fluxes, respectively; ω_e is the electric speed; and ω_r is the rotor mechanical speed.

The torque equation is given by the following Equation (11), taking Equation (3) into account:

$$T_e = \frac{3p}{4} \frac{L_m}{L_r} (\Psi_{rd} i_{sq} - \Psi_{rq} i_{sd}) \tag{11}$$

where p is the number of poles, L_m is the magnetizing inductance, L_r is the rotor inductance, Ψ_r is the rotor flux and i_s is the stator current. The subscripts d and q correspond to the axes of the component.

To ultimately obtain the model used for vector control, it is necessary to assume that the quadrature component of the flux is negligible, $\Psi_{rq} \approx 0$. As a result, $d\Psi_{rq}/dt \approx 0$, which means that the rotor flux is primarily composed of the direct rotor component. When this happens, the d and q components of the stator current are considered uncoupled. Consequently, the three-phase induction motor operates quite similarly to a separately excited DC motor.

In this way, and taking into account Equation (11), the electromagnetic torque in the stationary state of the induction motor is described by the following Equation (12).

$$T_e = \frac{3p}{4} \frac{L_m}{L_r} \Psi_{rd} i_{sq} \quad (12)$$

On the other hand, starting from the stator and rotor voltage Equations (9) and (10) and assuming once again that $\Psi_{rq} \approx 0$, the following expressions in their d - q components are obtained (Equations (13) and (14)).

$$v_{sd} = R_s i_{sd} + \sigma L_s \frac{di_{sd}}{dt} + \frac{L_m}{L_r} \frac{d\psi_{rd}}{dt} - \omega_e \sigma L_s i_{sq} \quad (13)$$

$$v_{sq} = R_s i_{sq} + \sigma L_s \frac{di_{sq}}{dt} + \omega_e \frac{L_m}{L_r} \psi_{rd} + \omega_e \sigma L_s i_{sd} \quad (14)$$

The obtained equations of voltage and torque are then use for the FOC, where the flux and torque components are decoupled, leading to independent control using quadrature axis or direct axis currents. Lastly, the specifications of the induction motor used in this paper are presented in the following Table 1.

Table 1. Induction motor specifications.

Feature	Value	Unit
Rated Power at 50 Hz	370	W
Rated Speed	2780	rpm
Rated Current (230 V)	1.7	A
Starting Current	4.56	A
Power Factor	0.83	-
Starting Torque	3.9	Nm
Maximum Torque	4.55	Nm
Rotor Inertia	3.5×10^{-4}	kgm ²
Nr. of Pole pairs	1	-
Statoric Phase Resistance	24.6	Ohms
Rotoric Phase Resistance	16.1	Ohms
Magnetizing Inductance	1.46	H
Electrical Time Constant	1.62×10^{-3}	s

2.3. Lithium-Ion Battery

Lithium-ion batteries (LIBs) emerged relatively recently, making their commercial debut in the 1980s. Since then, both their chemistry and technology have undergone significant advancements, establishing them as a superior choice over older rechargeable batteries like nickel cadmium (NiCd). The first types of Li-ion batteries used were lithium cobalt

oxide (LiCoO₂) batteries, but, during the 1990s, there were reports of these igniting. Therefore, they have since been replaced by safer alternatives such as lithium iron phosphate (LiFePO₄) and lithium nickel manganese cobalt oxide (LiNMC) batteries [33].

Lithium-ion batteries offer several key benefits, including the following.

1. **High Energy Density:** Lithium-ion batteries provide a high energy-to-weight and energy-to-volume ratio, making them efficient at storing and delivering power.
2. **Long Cycle and Calendar Lifetimes:** They have a longer lifespan in terms of both the number of charge cycles that they can endure and their overall calendar life.
3. **Fast and Efficient Charging:** Lithium-ion batteries can be charged quickly, and their charging process is highly efficient, minimizing energy waste.
4. **Low Self-Discharge Rate:** These batteries have a low rate of self-discharge, allowing them to retain stored energy for extended periods without significant loss.
5. **No Need for Upright Position:** Unlike some other battery types, lithium-ion batteries do not require a specific orientation and can be installed in various positions.
6. **Low Maintenance:** Lithium-ion batteries are relatively maintenance-free, reducing the need for regular upkeep.
7. **Minimal Voltage Sag:** They maintain a stable voltage output under load, ensuring consistent performance.

However, LIBs face limitations in meeting the escalating demands for energy storage and have essentially approached their theoretical capacity limits. To support the extended range of electric vehicles and facilitate the integration of renewable energy systems into smart grids, further enhancements are imperative in terms of their lifespan, safety, cost-effectiveness and environmental impact.

While LIBs possess advantageous characteristics like a high voltage and extended cycle life, optimizing the current battery chemistry and developing novel electrode materials could play a pivotal role in reducing manufacturing costs and lessening the environmental footprint associated with LIB production [34].

Battery systems that are engineered to succeed today's lithium-ion battery technology, with the capacity to fulfill the demands of energy-intensive applications, are commonly known as "post-lithium-ion batteries". Nevertheless, they are batteries in their early stages, and since the experiments conducted aim to compare different controllers, the most commonly used conventional lithium-ion batteries in electric cars to date, specifically lithium cobalt, are chosen [35]. The one used in this work is described in Table 2.

Table 2. Lithium cobalt battery specifications.

Feature	Value	Unit
Parameters		
Type	Ion-Lithium (Cobalt)	-
Nominal voltage	400	V
Rated capacity (Ah)	12.5	Ah
Initial SOC	100	%
Battery response time	30	s
Discharge		
Maximum capacity	125	Ah
Cut-off voltage	300	V
Fully charged voltage	465.59	V
Internal resistance	0.032	Ohms
Capacity at nominal voltage	113.15	Ah

3. Control Strategy Design

3.1. Performance Metrics

The determination of the best performance was not only based on graph analysis, but also on numerical reasoning. In this case, since the objective was to track a reference, error-based metrics were taken into account. In real time, the integral of the absolute error (IAE) was calculated in order to obtain suitable control parameters based on the minimization of this metric. Other parameters that were calculated after the data collection were the root mean squared error (RMSE) and the relative root mean squared error (RRMSE), which are also commonly used in tracking problems [36,37]. The three previous metrics are described in Equation (15).

$$\begin{cases} IAE = \sum_{i=1}^N e_i \Delta t \\ RMSE = \sqrt{\frac{1}{N} \sum_{i=1}^N (e_i)^2} \\ RRMSE = \sqrt{\frac{\sum_{i=1}^N (e_i)^2}{\sum_{i=1}^N (r_i)}} \end{cases} \quad (15)$$

where Δt is the sampling time (set to 5×10^{-5} s), N denotes the points gathered for calculation and r_i is the i -th reference point.

3.2. Sinusoidal Pulse Width Modulation

Sinusoidal pulse width modulation (SPWM) is a widely used technique in power converters for AC drive systems. The modulator is an electronic circuit that converts an analog signal into pulses, which control the electronic switches of the inverter. Thus, if the modulator's input is provided with the desired reference voltages of the three branches V_{sABC} from the inverter, the modulator generates the necessary pulses to achieve this objective.

A modulator consists of two voltages: the carrier and the fundamental. The fundamental is the reference voltage that is desired to be reproduced by the inverter, while the carrier is a triangular voltage that needs a frequency and amplitude higher than the fundamental. The fundamental is a sinusoidal voltage, and the carrier is typically a triangular voltage [38].

The modulator relies on a comparator that compares the two voltages, the fundamental and the carrier, and provides two possible output values. In a three-phase system, such as that of the induction motor, each branch is associated with a comparator, where the fundamental is a sinusoidal voltage phase-shifted by 120 degrees compared to the other two fundamentals, and the carrier is common to all branches. A schematic is given in Figure 2.

Once the comparison is completed, the switching states for each pole can be determined according to the following rule:

- $V_s(\text{Voltage reference}) > V_t(\text{Triangular carrier})$: Upper switch is turned on (pole voltage = $V_{dc}/2$);
- $V_s(\text{Voltage reference}) < V_t(\text{Triangular carrier})$: Lower switch is turned on (pole voltage = $-V_{dc}/2$).

Thus, the signal provided by the inverter is a chain of pulses whose fundamental component is the replica of the fundamental applied at its input (see Figure 3). In this way, the amplitude V_m of the output signal of the inverter is described as in the following Equation (16).

$$V_m = m \frac{V_{DC}}{2} \quad (16)$$

where m is the modulation index, described as the the ratio of the amplitude of the modulating wave to that of the carrier wave, shown in the next Equation (17):

$$m = \frac{V_s}{V_T} \quad (17)$$

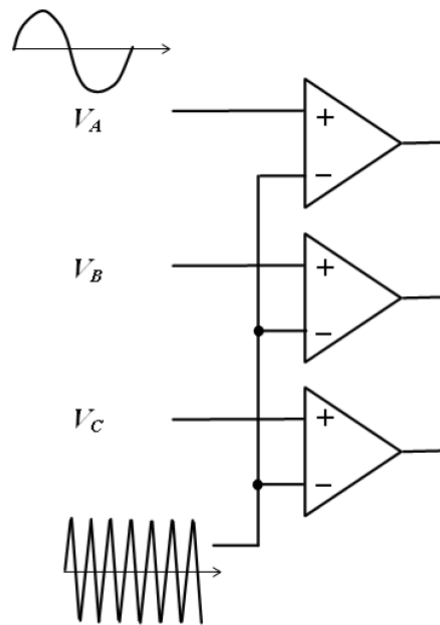


Figure 2. Three-phase sinusoidal modulation.

It has to be noted that the greater the difference between the fundamental frequency and the carrier frequency, the higher the order of the harmonics produced by the inverter, with the advantage that the machine's own inductance will filter them better, thus achieving currents more similar to a sine wave.

With respect to the other methods of pulse generation, the advantage of using the SPWM modulation over hysteresis control is that the currents provided by the inverter are of better quality than in the case of hysteresis control; they have a lower ripple, and the harmonic content is also lower.

In the case of space vector modulation (SVM), it is complicated to implement compared with SPWM due its requirement for complex computations in real time. Otherwise, SVM has a higher maximum modulation index of $m = 0.907$ compared to the SPWM, with $m = 0.785$. Nevertheless, the sinusoidal modulating wave of SPWM can be mixed with an appropriate amount of triplen harmonics (zero sequence components), which distorts the phase voltage references. In this way, the SPWM method can achieve the same modulation index as the SVM method [32].

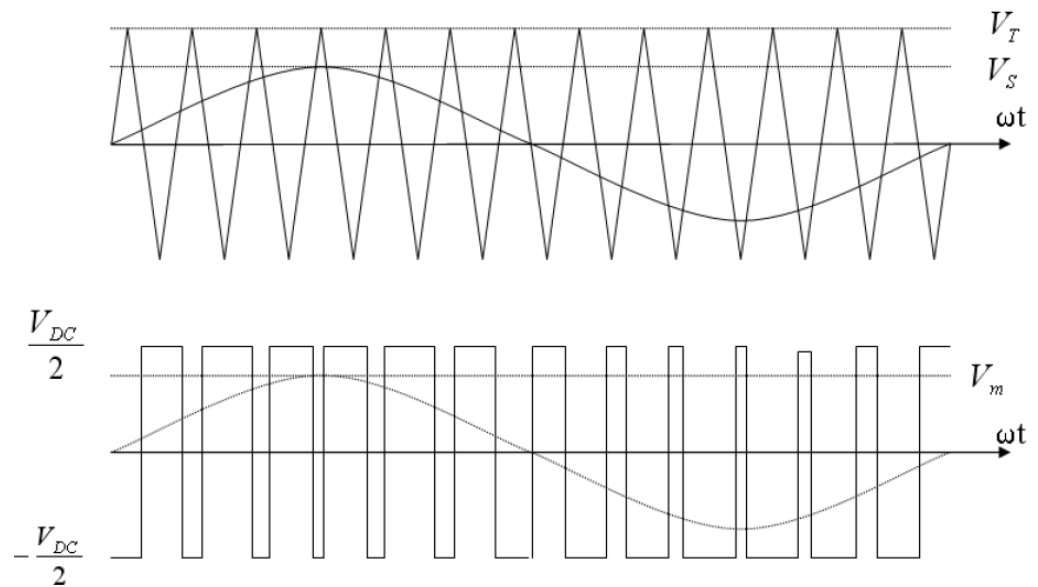


Figure 3. The fundamental and the carrier (top) signal provided by the inverter (bottom).

3.3. Model Predictive Control

Model predictive control (MPC) is an advanced control method that minimizes a cost function for a constrained dynamical system over a finite prediction horizon.

An MPC controller receives the current state of the plant at each time step and predicts its future state. It then calculates the sequence of control actions that minimizes the cost function over the prediction horizon by solving a restricted optimization problem, as shown in Figure 4. This optimization problem is based on the current system state and utilizes an internal plant model. Once the control sequence is determined, only the first control action is applied to the plant, while the subsequent actions are disregarded. This process is repeated in the subsequent time steps. The resulting control signal is then sent to the motor.

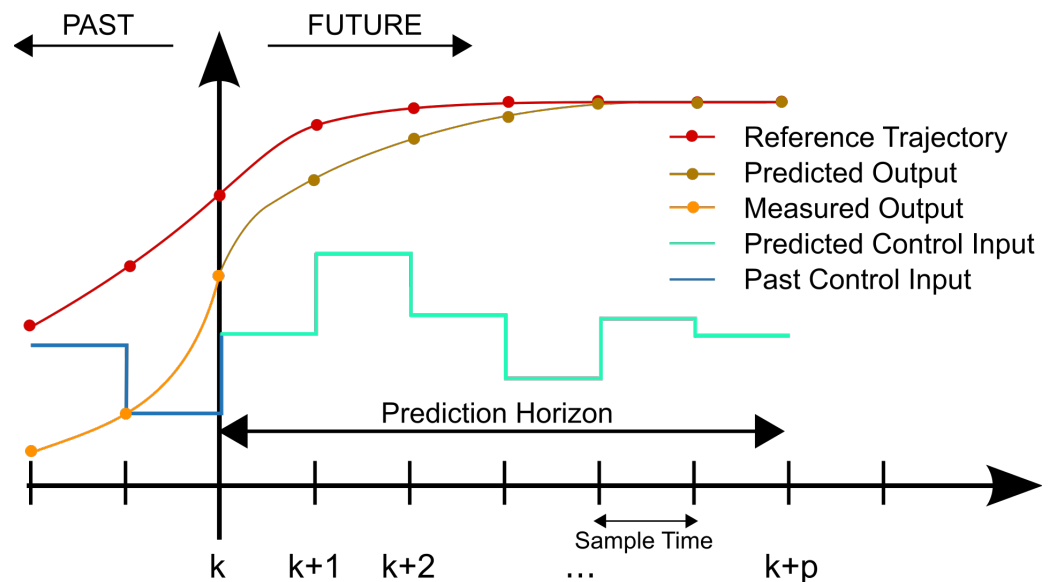


Figure 4. Model predictive control (MPC) control scheme.

This study employs the mechanical model of the plant to optimize the cost function of the MPC. The electric model is neglected since its dynamics are much faster, meaning that the system dynamics are primarily determined by the mechanical aspect [39]. The control input is driven by the speed reference and the speed feedback obtained from the

IM. Thanks to the internal mechanical model within the controller, the MPC calculates an optimal i_{sq}^* control signal to accurately track the provided reference. Considering Equations (4) and (12), the mechanical model of the IM motor can be described as follows:

$$j \frac{dw_m}{dt} + B_v w_m + T_L = \frac{3p}{4} \frac{L_m}{L_r} \Psi_{rd} i_{sq}(t - \tau) = K_t i_{sq}(t - \tau) \quad (18)$$

It can be described in discrete form as follows:

$$w_m(k+1) = \frac{T}{J} [K_t i_{sq}(k - \tau) - T_L - B_v w_m(k)] + w_m(k) \quad (19)$$

In both equations, a new term τ has been added that represents the delay of the input with respect to the output in the motor mechanical model. This term has been experimentally studied and its value obtained to be 0.1 ms.

The cost function utilized in the MPC is illustrated in Equation (20), where J_y represents the cost function of the reference tracking error (21) and J_ϵ represents the cost function of the constraint penalties (22). The cost function has the potential to be enhanced. For instance, a term can be added to restrict substantial control output changes between time steps. However, the implementation of such terms is not prioritized in this study in order to focus on reference tracking.

$$J(z_k) = J_y(z_k) + J_\epsilon(z_k) \quad (20)$$

Equation (21) expresses the tracking error cost function as the sum of the square of the differences between the reference and the predicted output weighted for all the steps from the instant to the prediction horizon. The importance of this error in the cost function increases as a function of the assigned weight, so that the higher the weight, the more aggressive controllers are obtained, at the cost of greater control efforts:

$$J_y(z_k) = \sum_{i=1}^p \{w_i [w_m^*(k+ik) - w_m(k+ik)]\}^2 \quad (21)$$

p refers to the prediction horizon, w_i is the weight of the tracking error, $w_m^*(k+ik)$ is the reference speed value in i steps in the future and $w_m(k+ik)$ is the analog in the future speed prediction.

Equation (21) formulates the tracking error cost function as the total weighted sum of the squares of the differences between the reference and the predicted output at each step from the present to the prediction horizon. This error's relevance in the cost function amplifies with the assigned weight, resulting in more aggressive controllers with higher weights but at the price of increased control efforts.

$$J_\epsilon(z_k) = \rho_\epsilon \epsilon_k^2 \quad (22)$$

where ρ_ϵ is the constraint violation penalty weight and ϵ_k the slack variable at control interval k .

The MPC has been designed experimentally to find the optimal design parameters, looking for the best result of the IAE parameter. These parameters are shown in Table 3. The restrictions on the maximum and minimum torque that can be applied come from the restriction of the motor taken as a reference to develop the model, as shown in Section 2.2.

Table 3. MPC controller's design parameters.

Parameters	Values
Sample Time	0.001 s
Prediction Horizon	30
Control Horizon	3
Torque Restriction	−4.55, 4.55 Nm

3.4. PID

Proportional integral derivative (PID) has been selected to perform a comparison with the MPC controller's performance. PID is a widely used simple and classic controller that is well known in academia and industry. PID controllers are based on feedback loops to calculate the action. Nevertheless, the simplicity that makes it so widely used and easy to implement limits the performance of the controller. Unlike the MPC, it lacks the ability to anticipate future states, so worse performance is expected.

The implementation of the PID control has been carried out using the blocks included in Matlab SIMULINK and the tuning tool that it includes. Equation (23) shows the implementation of the PID controller for discrete systems:

$$u(k) = K_p e(k) + k_i \sum_{i=1}^k e(i) \Delta t + K_d [e(k) - e(k-1)] \quad (23)$$

where $u(k)$ is the control action, $e(k)$ and $e(k-1)$ are the error in the actual and previous time steps, Δt is the time step and k_p , k_i and k_d are the proportional, integral and derivative constants.

The tuning process of the PID has been performed through the minimization of the IAE parameter, as mentioned in Section 3.1. In this way, the parameters for the PID controller have been chosen, as shown in Table 4.

Table 4. Design parameters for the PID of the speed loop.

Constant	Value
K_p	0.2
K_i	0.27
K_d	0

On the other hand, as will be described in Section 4.2, apart from the speed loop, there is also a current loop underneath, where two PI controllers give the voltage values on the d- and q-axes to reach the reference currents. The PIDs have been tuned similarly to the PID for the speed loop, specifically by minimizing the IAE parameter and taking into account that the current loop must be faster than the speed loop. Therefore, the band width in the current loop is 10 times larger than in the speed loop, obtaining the parameters specified in Table 5.

Table 5. Design parameters for the PIDs of the current loop.

Constant	Value
K_p	45
K_i	100
K_d	0

4. Results

The results are divided into experiments performed in simulation and those performed in HIL. For both cases, it is worth describing in general terms the control scheme used for the motor speed tracking shown in Figure 5. In this figure, it can be seen that the blocks represented are divided into three colors. This division corresponds to the different sample rates at which they are executed. As mentioned in Section 2.1, due to the capacity limits of the DS1202, the motor and the power electronics groups run at a sample rate of 5×10^{-5} s (blue). The control section, on the other hand, runs on the DS1104 board at a maximum sample rate of 1×10^{-4} s. However, as can be seen in Figure 5, the control section is divided into two other groups: the current loop (magenta), which is the one that ultimately generates the required motor voltage input signal that provides the current demanded by the speed controller, must always move faster than the upper speed loop (yellow), where the controllers that have been discussed are located. In addition, the current loop must be slower than the system to be controlled, i.e., the electric motor. For this reason, and conditioned by the limits of the boards, the sample rates chosen are the following:

- Electric motor and power electronics (blue): 5×10^{-5} s;
- Current loop (magenta): 1×10^{-4} s;
- Speed loop (yellow): 1×10^{-3} s.

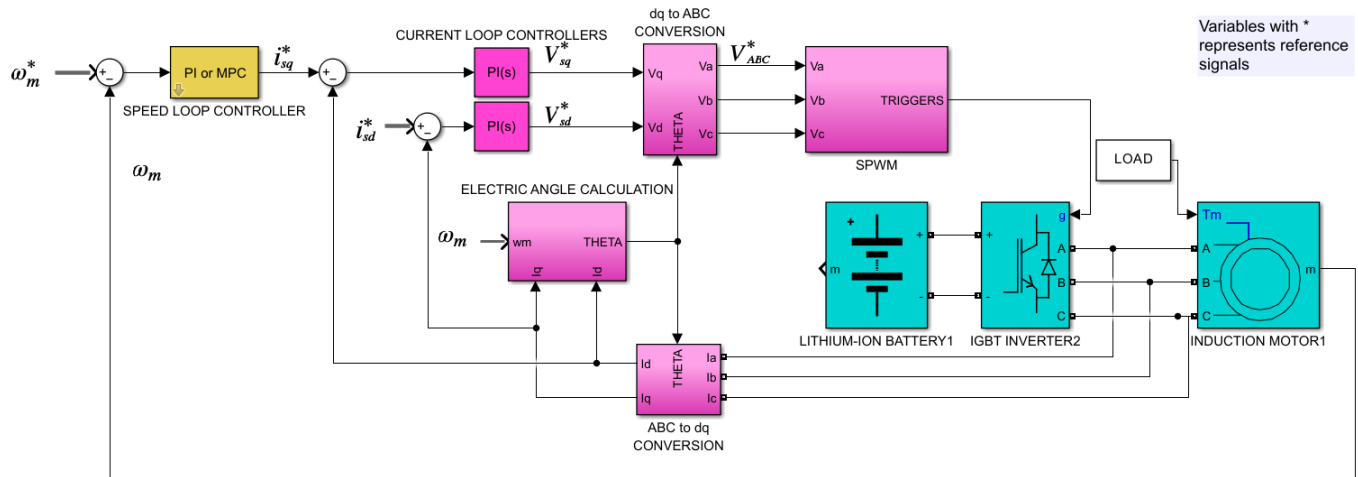


Figure 5. Block diagram of IM speed control with FOC control method. * on a variable represents the desired value.

4.1. Simulation Results

First, the designed MPC and PI have been tested through Matlab SIMULINK simulations. As observed in Figure 6, the controllers must follow a step signal that reaches 100 rad/s speed in the first second. Moreover, at second 2.5, a torque of load of 0.6 Nm has been added to compare the robustness of the controllers, simulating an increment in the wind speed opposite to the vehicle movement.

As can be seen, both controllers reach the speed target almost at the same time, although the MPC reaches it 0.015 s faster. They both show a response with no overshoot. However, as can be seen in the magnified figure, in the stationary state, the PI oscillates above the 100 rad/s threshold, reaching 101.5 rad/s, 67% higher than the one reached by the MPC. As described in Section 2.1, the sample rate is limited to 2×10^{-5} s and therefore the speed given by the IM presents discontinuous values between samples, which results in some chatter (noisy signal). It should be noted that the control signal cannot be changed between samples, so the larger the sampling period is, the larger overshoot will be. This should be compensated for in the next sample time generating an undershoot and so on. Therefore, in our case, where the output signal presents some oscillations, the PI, which uses the speed tracking error to calculate the control signal, suffers more from these

oscillations in the speed signal. The MPC, in contrast, is less susceptible to this because it takes into account a model of the system in order to calculate the system output in the next sample time; therefore, it can surmount these drawbacks in the prediction and optimization process. The predictive nature of MPC allows it to anticipate changes in the system and adapt its control actions accordingly.

As noted before, in second 2.5, the electric motor is perturbed with 0.6 Nm load torque, for which the controllers try to compensate. As expected, the MPC works better against perturbations, since it shows almost no reduction in speed, only dropping to 98.2 rad/s and reaching the setpoint again 0.05 s later. This is due to the MPC's inherent ability to predict future states, resulting in more robust control. The PI, on the other hand, does show a considerable drop in speed of 5.4 rad/s, from which it is unable to recover until 0.75 s later.

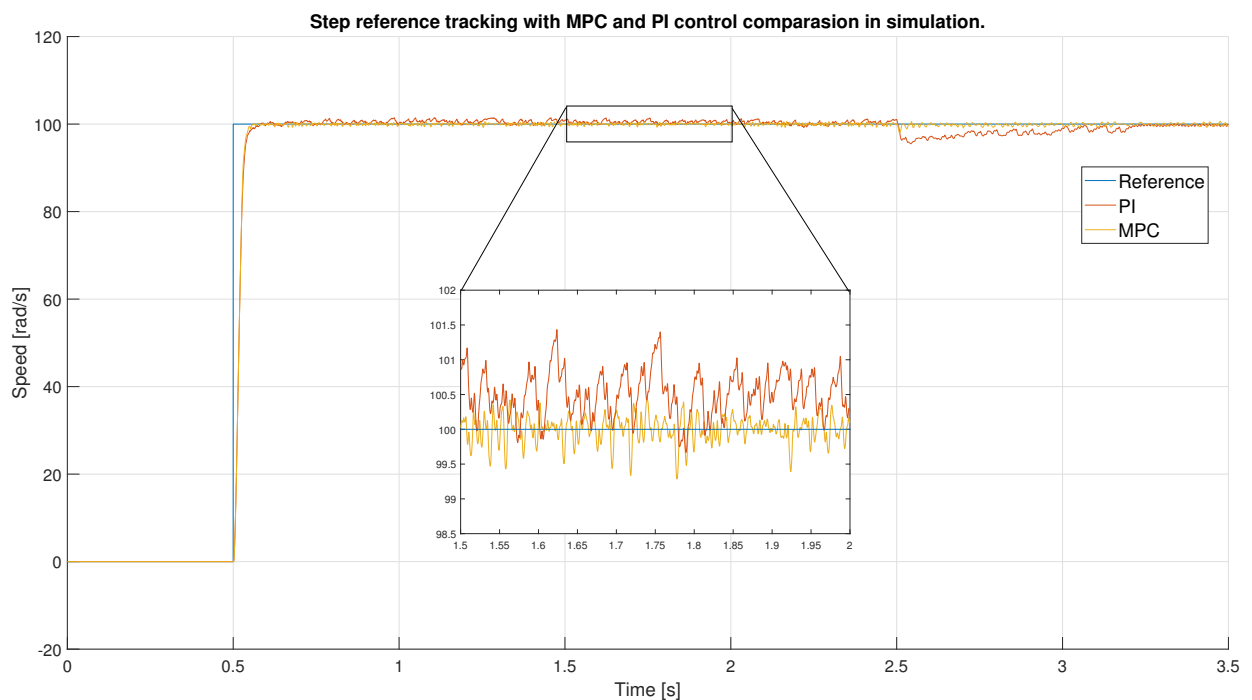


Figure 6. Simulation speed tracking performance of MPC and PI.

Looking now at Table 6, where the results of the performance metrics are shown, it can be seen that, in all metrics, the MPC outperforms the PI, which is consistent with Figure 2 seen above. In fact, the MPC shows an improvement of 48.2% and 2% in the IAE and RMSE metrics, respectively. The great difference between these two metrics based on the error can be explained by looking again at Figure 2. The response of the controllers remains in steady state up to 80% of the time, where the error does not exceed 1 rad/s. When we calculate the square of a value less than 1, it decreases. For values greater than 1, on the other hand, the opposite happens. This is why the RMSE parameter, which squares the errors, makes the differences between the two controllers during steady state relatively insignificant. It is only when the torque load is introduced into the system that the RMSE value can effectively be differentiated. The IAE, on the other hand, does not square the error; therefore, the difference that is observed in steady state has a greater influence on its value.

Table 6. Simulation performance metric results.

		IAE	RMSE	RRMSE
Simulation	PI	4.8090	18.3370	0.6199
	MPC	2.5293	17.9799	0.6078

4.2. Hardware in the Loop Results

Once the simulation was concluded, the controllers were tested in a HIL environment, which, as described in Section 2.1, consisted of two dSPACE DS1104 and DS1202 boards, where the control section and the electric motor together with power electronics were implemented, respectively, as shown in Figure 7.

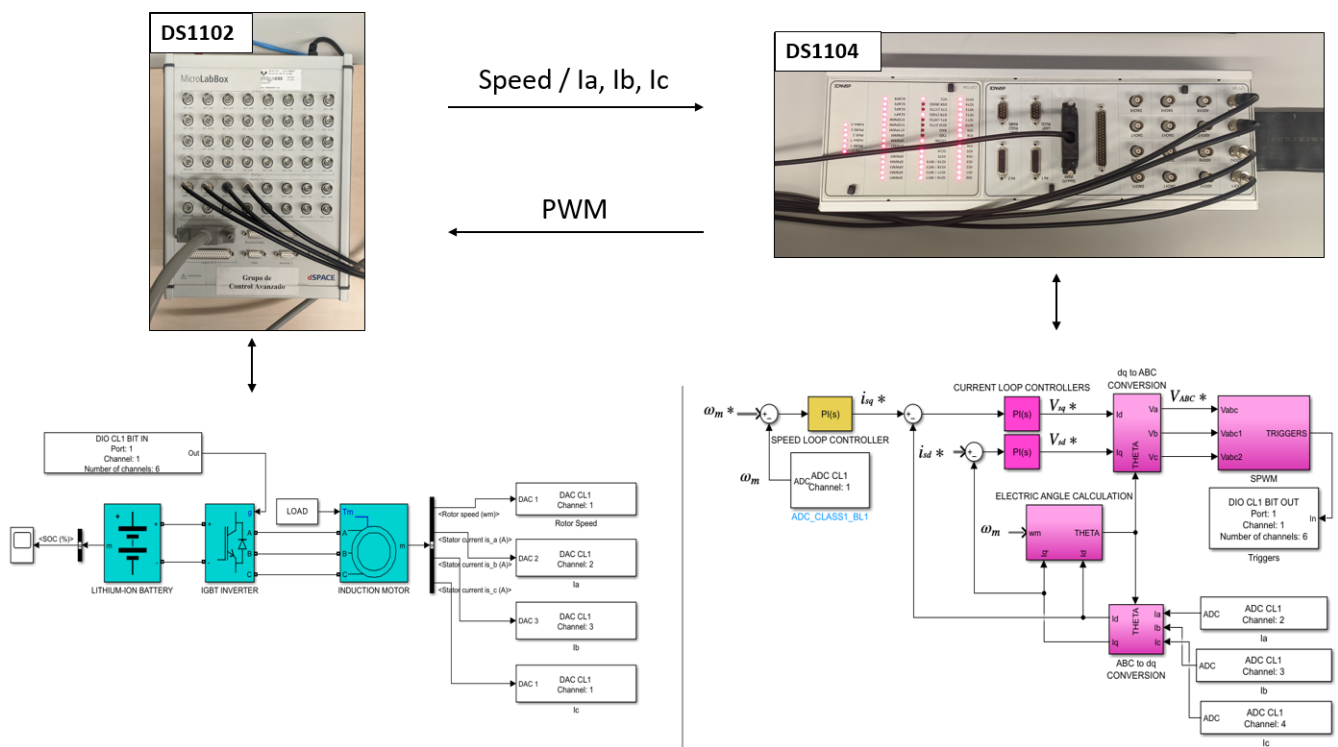


Figure 7. HIL configuration.

The HIL tests consist of four experiments. The first one has the same tracking reference as the simulation experiment, a step signal that moves from 0 to 100 rad/s. The same 0.6 Nm torque load is also used to observe the robustness of the controllers. The use of the same experimental conditions for HIL is due to the interest in observing the differences that may exist between the simulation and an environment that is closer to a real system.

As can be observed in Figure 8, both controllers show a similar response when the step signal enters at second 0.5. This continues until they reach the setpoint, at which point the PI describes an underdamping response reaching 101.4 rad/s. Both controllers behave in the same way in the raising time due to the limitations of the motor, since they are both providing the maximum torque signal of 2 Nm. It is only at the moment of reaching the setpoint that they are differentiated, where the MPC is able to lift the setpoint and remain stable from the first moment. The PI, on the other hand, takes 2.4 s longer to reach a stationary state. Not only is the PI slower to reach the target, but, already in the stationary region, the PI is more susceptible to small perturbations that affect the speed, as can be seen in the magnified image. The PI shows jumps of 0.3 rad/s, while the MPC remains stabilized at the setpoint. However, the MPC shows small oscillations that do not exceed

0.12 rad/s of amplitude, caused by the delays suffered by the speed reading signal, in turn caused by the filters used to reduce noise.

After second 6.5, at which the load torque is applied, the MPC still maintains the speed of 100 rad/s, with a small mismatch of 1 rad/s, and takes 1 second to stabilize again, compared to the 6.7 rad/s speed decrease shown by the PI. In addition, the PI is not able to properly correct it and has a 5 rad/s overshoot until it reaches stability at 100 rad/s, thus taking 4.5 s longer than the MPC to stabilize again.

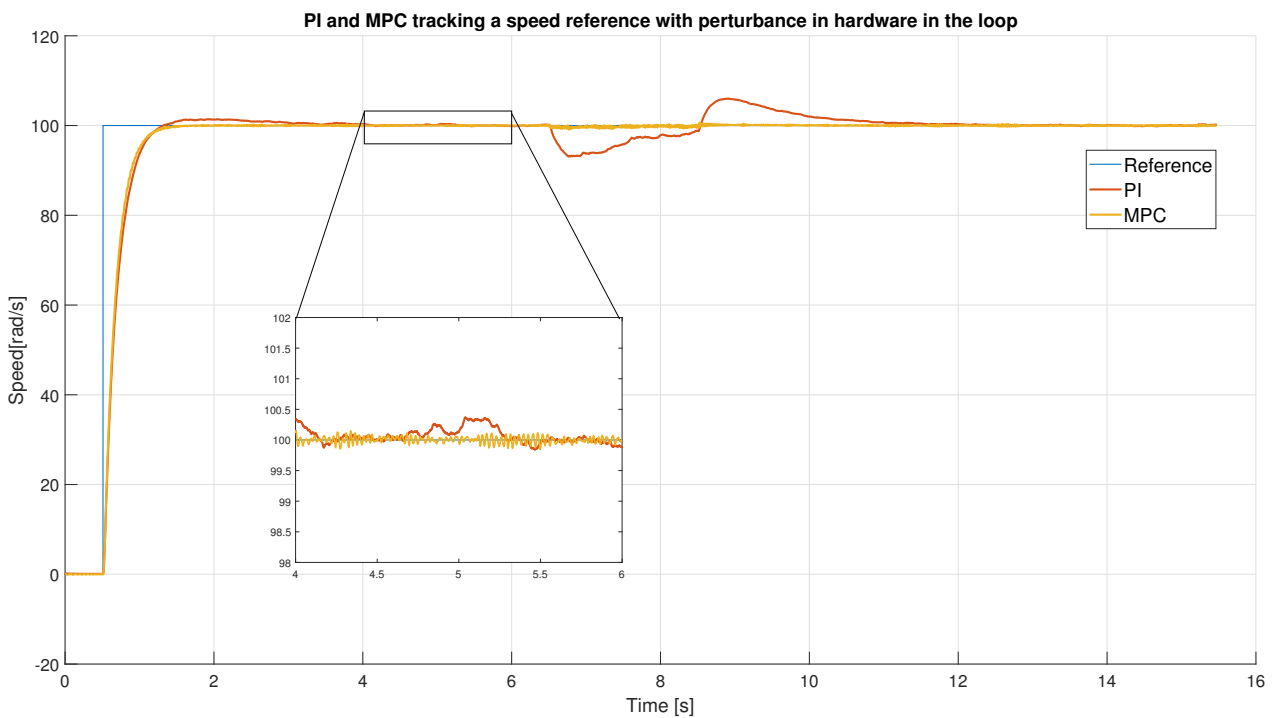


Figure 8. HIL speed tracking performance of MPC and PI.

In order to obtain the numerical improvement of the MPC, Table 7 is included, as for the simulation, where the results of the performance metrics are shown. Once again, the MPC outperforms the PI in all metrics, achieving an improvement of 51.13% and 6.67% in the IAE and RMSE, respectively. It should be noted that, in improvement terms, the simulation and HIL experiments show similar results. However, the PI’s performance is worse compared to the MPC in HIL, so the improvements are consequently higher.

Table 7. HIL Performance metric results.

		IAE	RMSE	RRMSE
Hardware in the loop	PI	38.0611	8.2678	0.8408
	MPC	18.6012	7.7160	0.7846

Comparing now the simulation results with those obtained with HIL, the main short-coming to be mentioned is the noise and the delays in the case of HIL. This last one is due to the more restrictive low-pass filters used on the read signals, such as the mechanical speed and stator currents. This fact causes, in the first instance, a smaller raise time in the simulation compared to the one described in HIL, 1.056 s faster specifically. The controllers give their maximum torque during the raise time in both cases, but the more restrictive filters used in HIL do not allow for such a fast response.

Another cause of the more restrictive filters is observed in the stationary state, where the responses of the HIL controllers show lower noise and oscillations, even with the added

noise from the wired signals, analog signal measurements and AD/DA conversions. In simulation, the MPC reaches 100.1 rad/s, while, in HIL, the same controller reaches up to 100.5 rad/s, an increase of 0.4 rad/s. In the case of the PI, the increase is even higher, 1.1 rad/s. This fact indicates that even with the noise added by wire transmission, the designed filters attenuate the signal optimally, with the drawback of slower responses. In fact, the PI used in HIL has been modified to mitigate the effect of the filters and hence compensate for this delay in the response. Thus, the PI has been designed to be more aggressive and the response obtained when the reference signal changes in second 0.5 shows an overshoot of 1.4 rad/s.

This new PI design also affects the response of the model when the 0.6 Nm of load torque is added to the system. As already mentioned, the filters slow down system responses and a more aggressive PI allows for faster responses, with the drawback of forming larger overshoots. In fact, the PI shows, in HIL, a drop of 1.7 rad/s, compared to the simulation PI. In addition, the filters cause it to reach the setpoint 1.33 s slower.

The MPC, on the other hand, is able to show the same response in both experiments, even with the effect of the filters, making it a more robust option for instantaneous changes in the system and a better choice for systems with delays.

The second experiment sought to bring the IM to the nominal speed value of 290 rad/s and to determine the performance of the controllers. In addition, the maximum load torque was applied in the test to check how the controllers responded. It is worth mentioning that both the MPC and the PI were not modified, i.e., the parameters used for the speed reference of 100 rad/s were maintained. In this way, the adaptability of the controllers to operating points other than those for which they were designed could be tested.

As can be seen in Figure 9, the MPC reaches and stabilizes at the reference signal at second 4.42, while the PI reaches 290 rad/s at second 4.9 and shows an overshoot with a value of 484.4 rad/s. It also takes 2.2 seconds longer to stabilize than the MPC. This shows that the MPC outperforms the PI in tracking the nominal speed in both speed and accuracy, showing an improvement of 40.6% in rise time and 81.5% in settling time.

As previously discussed, in second 9.7, a value close to the maximum torque of 4.4 Nm is applied. In this case, the MPC is able to maintain the nominal speed but experiences a decrease of 37 rad/s, only to recover to the reference value at second 11.77. Conversely, the PI controller is more heavily affected by the maximum load torque, dropping down to 60 rad/s. Furthermore, it fails to maintain the nominal speed upon returning to it, reaching 640 rad/s before eventually stabilizing, 4.6 s after the MPC.

In this way, it can be asserted that the MPC, even when optimized for a speed of 100 rad/s, demonstrates optimal control even when subjected to the maximum load torque. On the other hand, the PI controller relies on parameters designed for a specific operating point, exhibiting significantly poorer performance compared to the MPC in terms of stabilization times and errors relative to the reference signal. Indeed, as is evident in Table 8, the MPC outperforms the PI in terms of the performance metrics, yielding an IAE value that is 8.4 times smaller and showing a 72% improvement in root mean square error (RMSE) and relative root mean square error (RRMSE).

Table 8. Nominal speed tracking performance metric results.

		IAE	RMSE	RRMSE
Hardware in the loop	PI	1061.9	105.7	14.45
	MPC	126.2695	29.56	4.04

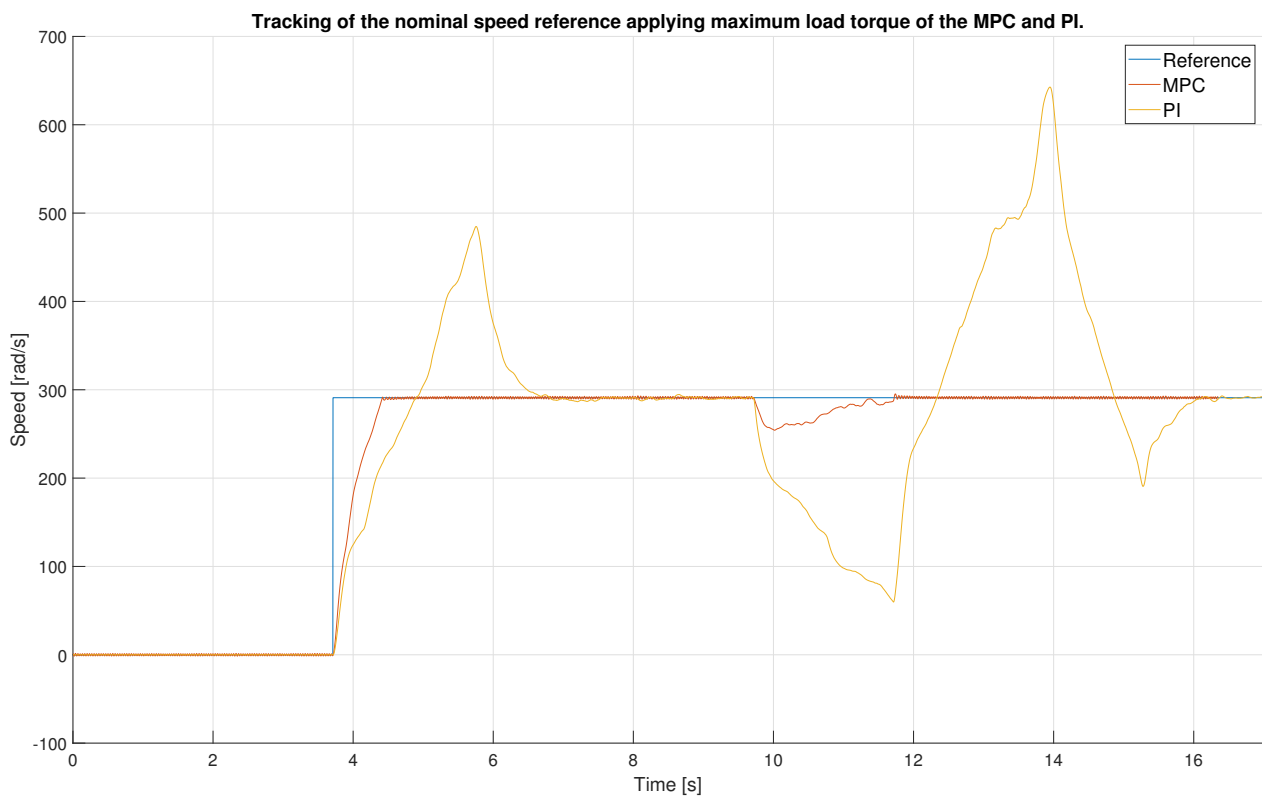


Figure 9. Tracking of the nominal speed reference of the MPC and PI when applying maximum load torque.

In a subsequent experiment, various reference speeds were selected to observe the total harmonic distortion (THD) exhibited by the currents in the stator of the IM. The current I_a was used as the signal for frequency analysis, allowing us to analyze its harmonics and extrapolate these findings to the other currents, i.e., I_b and I_c .

Figure 10 shows the current signal I_a when the motor speed is at 250 rad/s for both the MPC and PI control cases. It is clearly observed that it is not a perfect sine wave and has several harmonic components and some noise. This signal is used in the frequency analysis shown in the following Figures 11 and 12, corresponding to the MPC and PI controllers. In both cases, an initial peak corresponding to the fundamental frequency of 39.77 Hz is observed. Following this, a series of harmonics and noise can be seen in both figures, with the MPC showing initial harmonics of smaller amplitude compared to those of the PI, which reach an amplitude of 0.05. In the case of the PI, a peak in the fifth harmonic is also observed, reaching an amplitude of more than 0.1.

These results indicate that the MPC achieves a more ideal signal in the motor currents, which is consistent with the total harmonic distortion (THD) values observed in Table 9. In this table, several reference speed cases are presented, in which the MPC also achieves smaller THD values. It is worth mentioning that, at higher speeds, the fundamental frequency is higher, and, as a result, the frequencies considered for THD calculation are higher. This leads to a higher resultant THD value when considering the lower amplitude of the first harmonics compared to those at higher frequencies, as shown in the frequency analysis above. Nonetheless, the improvement percentage of the MPC remains consistent in all three cases, ranging between 40% and 65%.

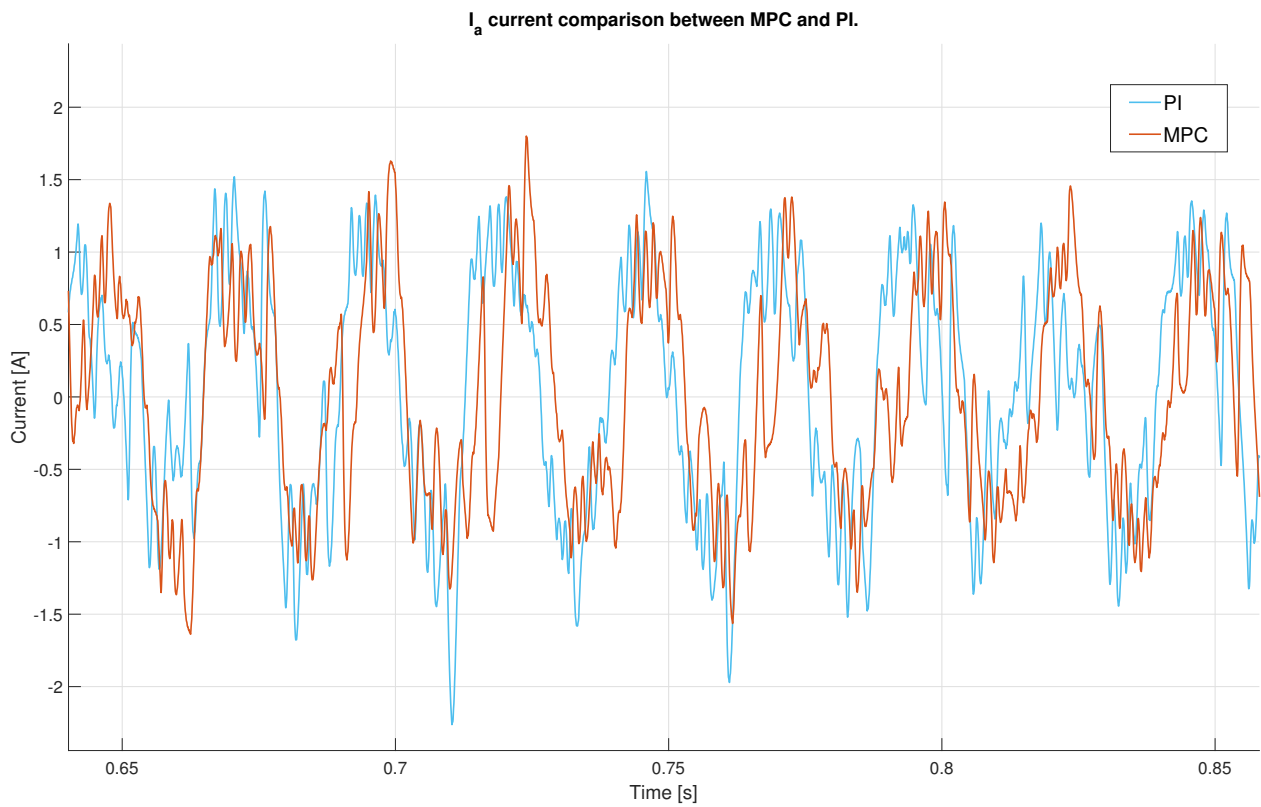


Figure 10. I_a current comparison between MPC and PI.

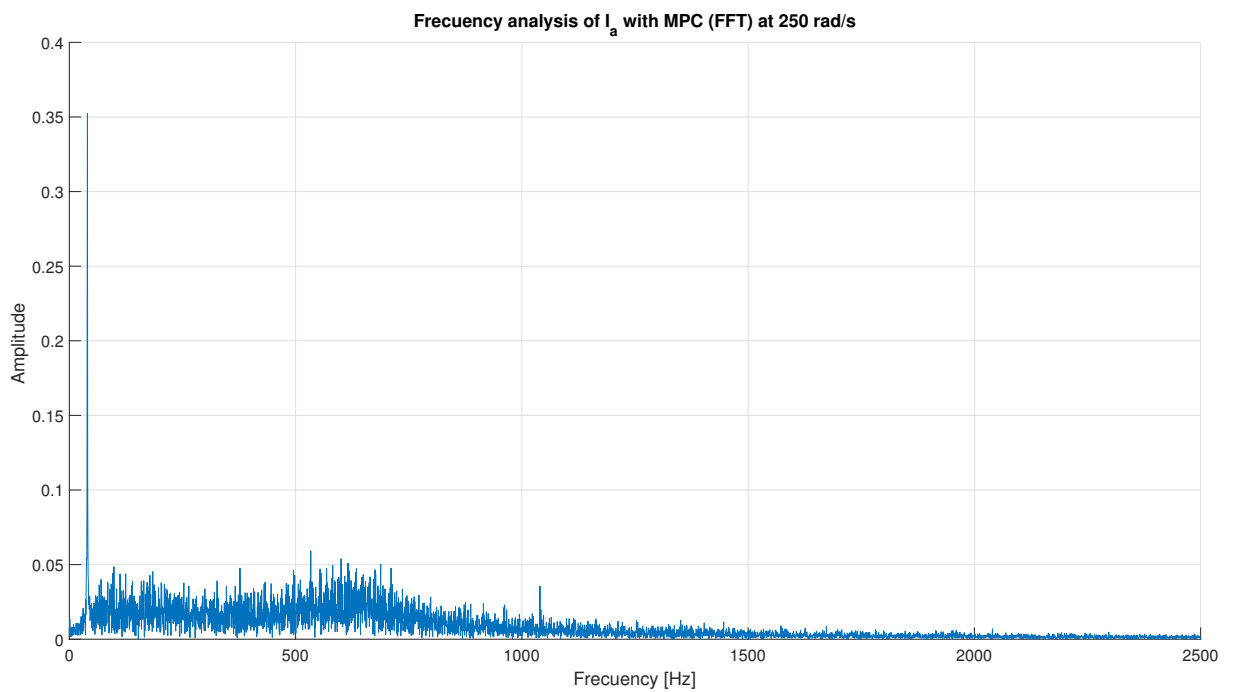


Figure 11. Frequency analysis of I_a with MPC (FFT) at 250 rad/s.

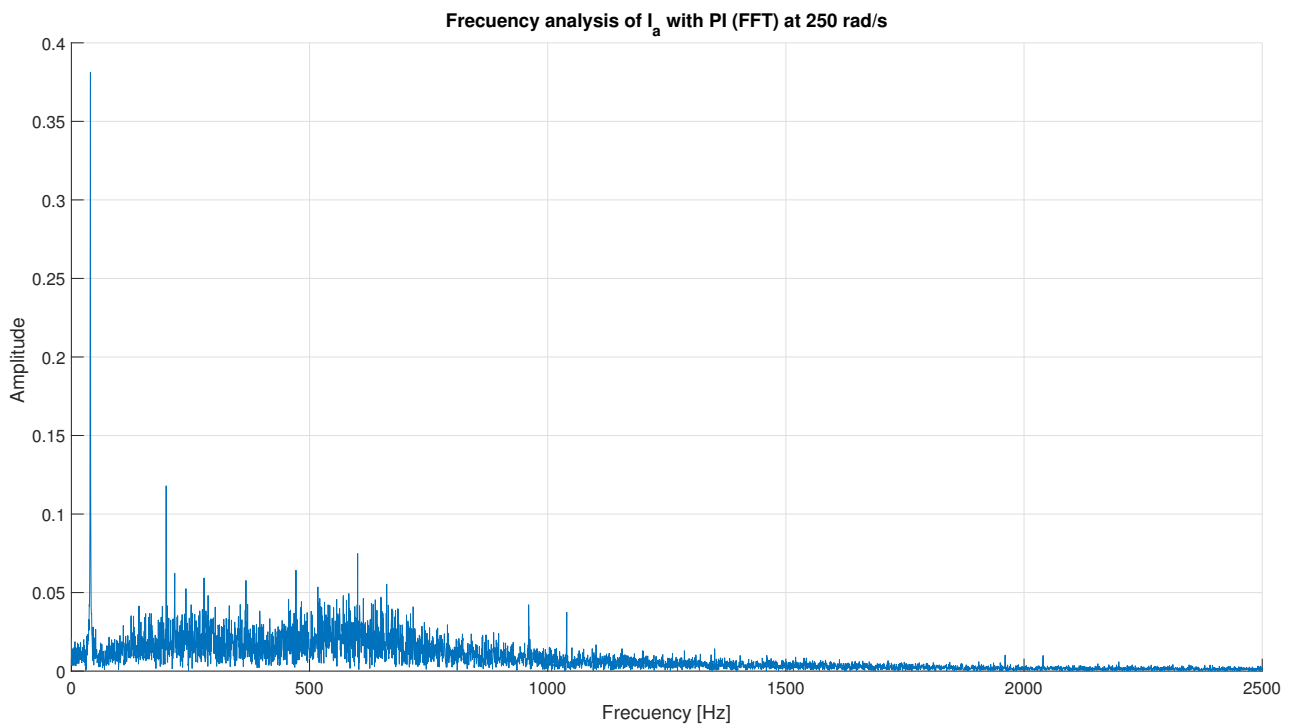


Figure 12. Frequency analysis of I_a with PI (FFT) at 250 rad/s.

Table 9. THD values for different speed references.

Speed Reference [rad/s]	THD [%]		Fundamental Frequency [Hz]
	MPC	PI	
100	4.21	9.03	15.9
200	7.52	18	31.82
250	26.29	40.15	39.77

In a third experiment, the robustness of the MPC was tested by altering various parameters of the motor to be controlled. In the first test, the value of the rotor resistance was modified by 30% and 50%, and the motor was brought to its nominal speed. The results are shown in Figure 13, where the three cases are compared: the ideal motor, the motor with 30% larger rotor resistance and the motor with 50% larger rotor resistance.

In all three cases, the MPC exhibits similar behavior, although, when changing the rotor resistance, the MPC becomes 15.9% and 16.6% slower in reaching the reference, in the case of a 30% and 50% increase, respectively. This is because increasing the resistance results in a decrease in rotor current and, consequently, in the starting torque. This implies that the motor will take more time to reach the desired speed.

In a second test, the motor's inertia was modified, increasing its value by 30% and 70%. As can be observed in Figure 14, the increase in inertia was proportional to the slowness of the system in reaching the reference speed, 6% and 13.7% slower for 30% and 70% increases in inertia, respectively. This occurs because higher inertia means that the motor and the load that it drives are more difficult to accelerate or decelerate; they exhibit "resistance" to changes in speed. The motor must provide sufficient torque to overcome this inertia and reach the required speed, and the higher the inertia, the longer it will take to overcome this internal resistance and reach the desired speed. The MPC is unable to counteract this increase in inertia because it is heavily dependent on the model with which it has been designed and, therefore, does not account for changes in model parameters. However,

the performance of the controller is not seriously deteriorated due to the robustness of the MPC.

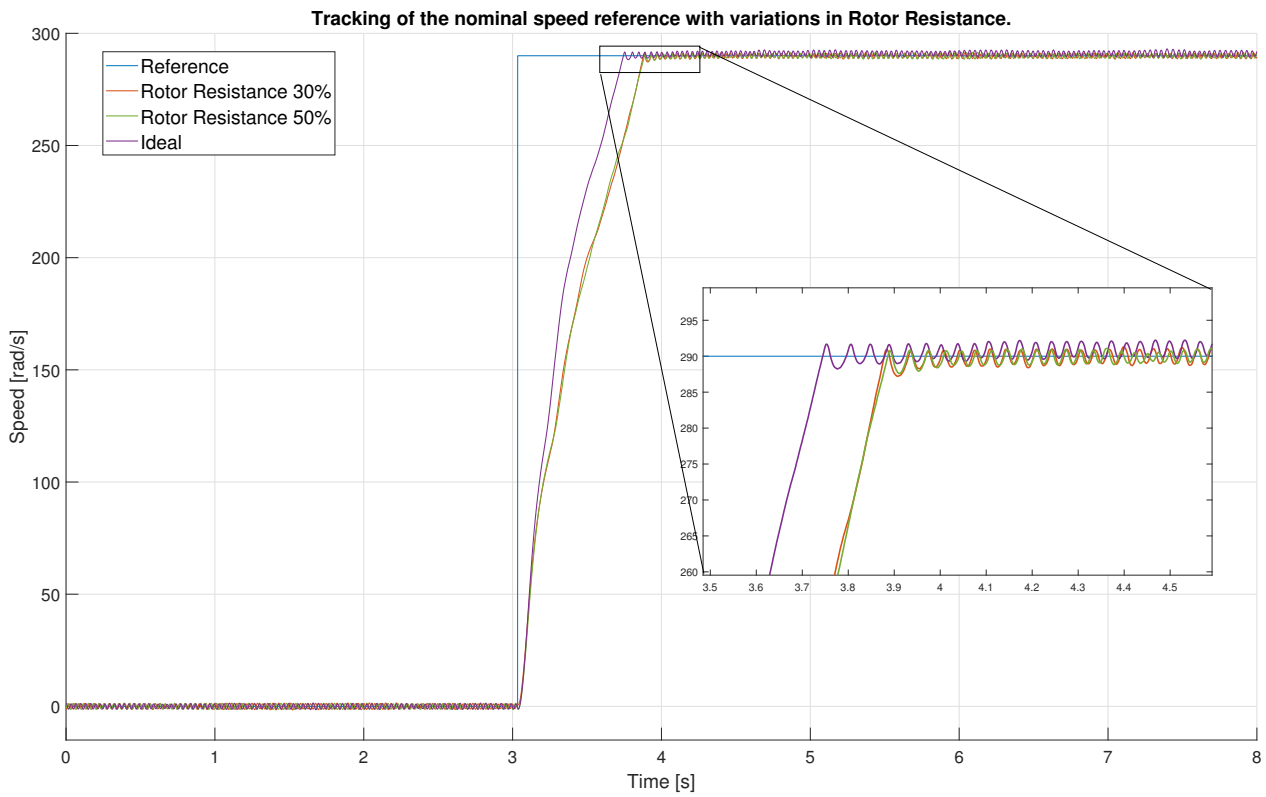


Figure 13. Tracking of the nominal speed reference with variations in rotor resistance.

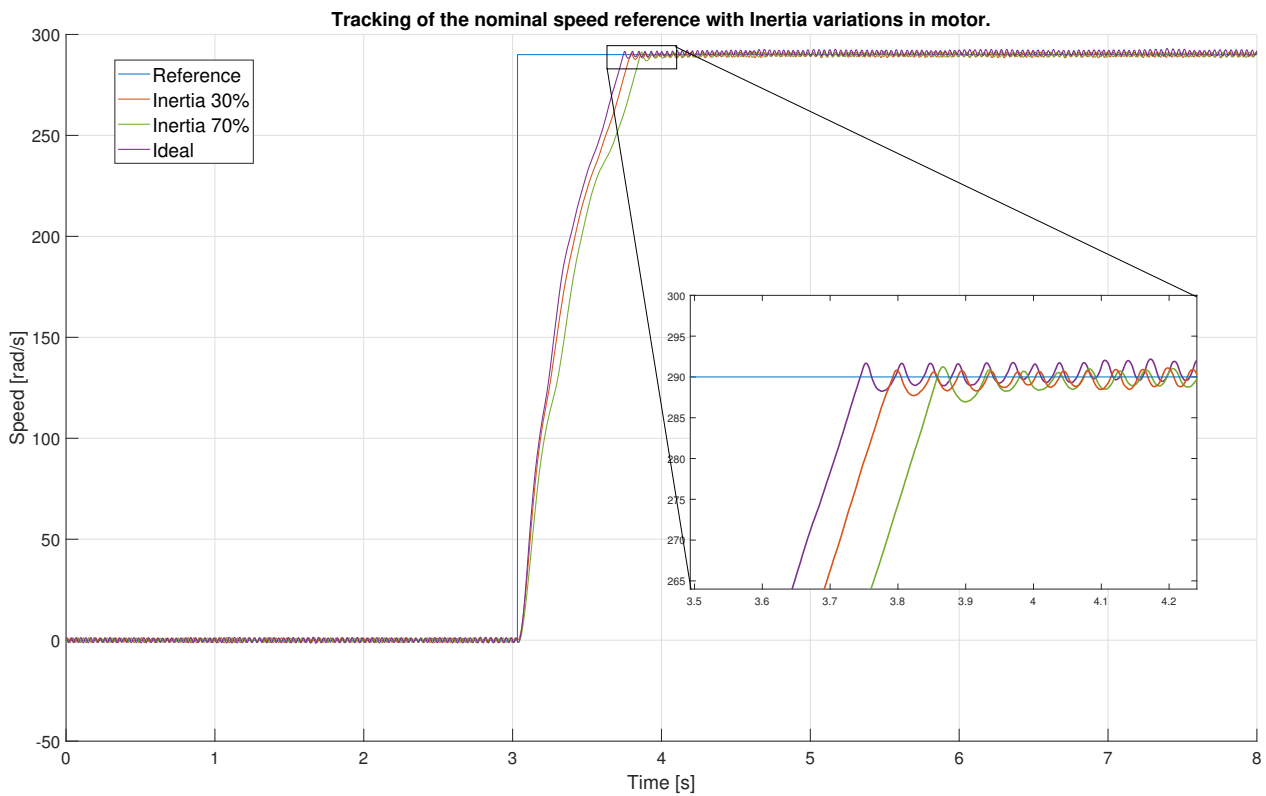


Figure 14. Tracking of the nominal speed reference with inertia variations in motor.

The last experiment consisted of a large test where the state of charge (SOC) of the lithium-ion batteries was observed. For this experiment, the induction motor velocity profile shown in Figure 15 was chosen and repeated in time until the batteries reached 20% of charge. This is the minimum value at which batteries should be maintained to extend their lifespan [40]. Figure 16 shows the SOC of the battery throughout the experiment, where the differences between the two designed controllers can be observed. In the first 3 h, the difference cannot be distinguished, but after the SOC reaches 60%, the MPC's SOC starts to extend above the PI line. At the end, the PI reaches 20% of the SOC after 8 hours, while the MPC has 20.835% left. This translates into 5.07 min more driving time.

It should be noted that the improvement in the MPC's performance is not remarkable in the area of battery reduction. This is due to the lack of use of any battery management techniques, as used by the authors of [41]. The only improvement in the MPC over the PI in terms of battery usage is obtained because the MPC shows a smoother response, since it reaches the speed setpoint without overshoot, as seen in the previous experiments, and it shows a less noisy response in the stationary state.

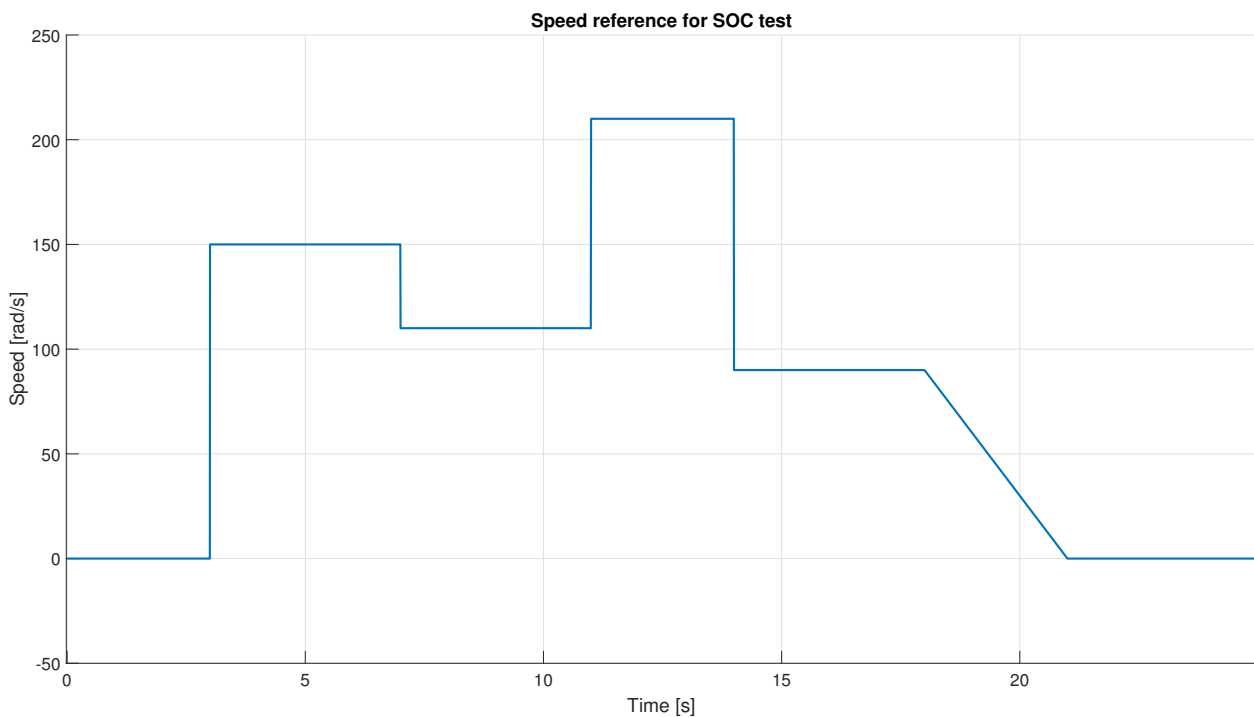


Figure 15. Speed reference for SOC test.

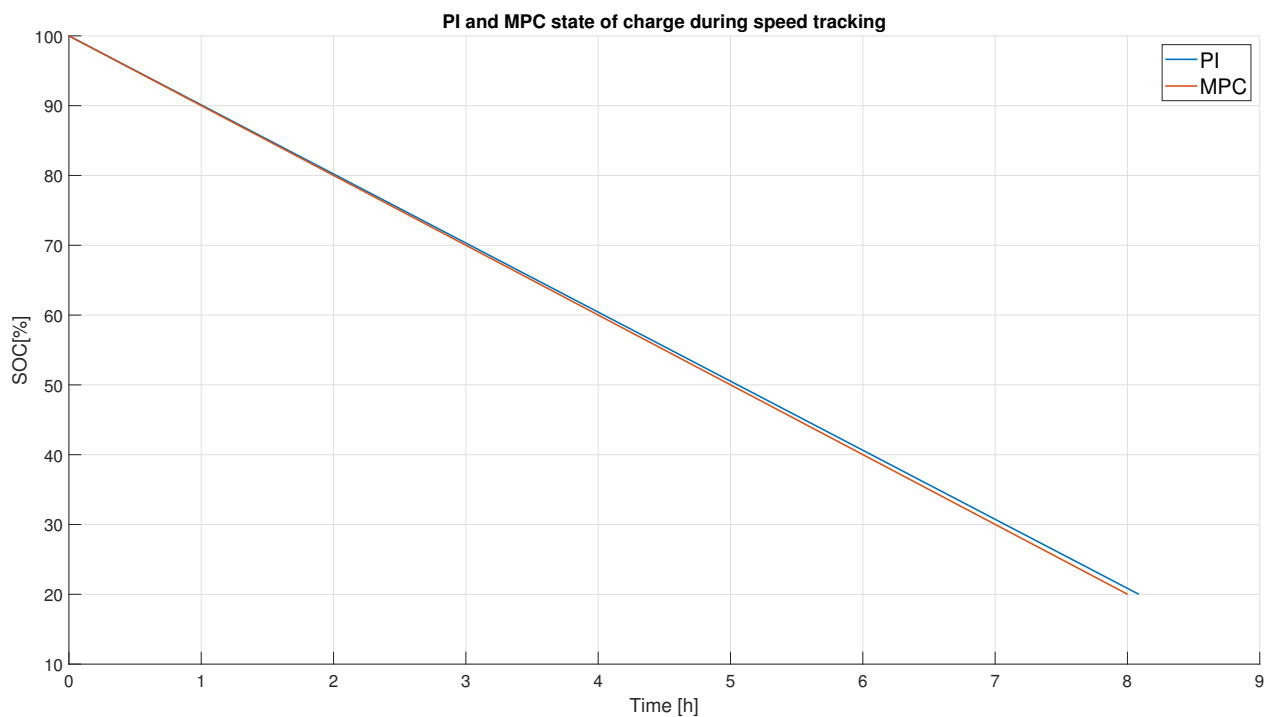


Figure 16. PI and MPC SOC during speed tracking.

5. Conclusions

The rise of electric vehicles has led to the reexamination of mature and established electric motor control in the industry, in pursuit of increased battery efficiency and control robustness. Within electric cars, the induction motor is the most widely used due to its low cost, robustness, little maintenance and reliability. To implement speed control for these motors, one of the most sophisticated methods is FOC. This is the control method used in this study due to the improvements that it offers compared to its main competitor, DTC, as described earlier, including reduced current ripple.

In this work, a CCS-MPC has been designed and compared to a conventional method of tracking a speed reference. Both simulation and real-time validation have been carried out in order to visualize the developed controller in different environments, and the results show that, in both cases, the designed MPC outperforms the conventional PI, as demonstrated by the performance metrics IAE, RMSE and RRMSE. In fact, the MPC shows an improvement of nearly 50% in both environments due to its robustness and predictive capacity, which allows it to show a smoother and more stable response. In addition, the experiment conducted on the SOC of lithium-ion batteries shows that the control performed by the MPC allows 5.07 min more driving time compared to the PI.

This work is expected to lead to a subsequent experiment where the created control scheme will be validated in a real induction motor together with a real three-phase inverter and another electric motor as a load in the tests. In the future, furthermore, it is intended to implement comparative tests with more differentiated control design variations by adding SOC management optimization or the control methods discussed in the Introduction of this article. The issue is that the variety of motors, control methods and controllers within the speed loop and current loop allow several configurations for vehicle propulsion systems, which are impossible to cover in one study; therefore, specific configurations must be chosen and worked with, as was the case in this work.

Author Contributions: Conceptualization, O.B., I.C. and J.U.; methodology, O.B. and J.U.; investigation, J.U.; software, J.U. and O.B.; writing—original draft preparation, J.U. and E.A.; writing—review and editing, J.U., O.B. and I.C.; visualization, J.U., E.A. and A.d.R.; supervision, O.B. and I.C.; project administration, O.B. and I.C. All authors have read and agreed to the published version of the manuscript.

Funding: This research received no external funding.

Data Availability Statement: Not applicable.

Acknowledgments: The authors wish to express their gratitude to the Basque Government, through the project EKOHEGAZ II; to the Diputación Foral de Álava (DFA), through the project CONAVANTER; to the UPV/EHU, through the project GIU20/063; and to the MobilityLab Foundation (CONV23/14. Proy. 16), for supporting this work.

Conflicts of Interest: The authors declare no conflict of interest.

Abbreviations

The following abbreviations are used in this manuscript:

EV	Electric Vehicle
EM	Electric Motor
IM	Induction Motor
PMSM	Permanent Magnet Synchronous Motor
BDCM	Brushed Direct Current Motor
PF	Power Factor
SPM	Switched Reluctance Motors
FOC	Field-Oriented Control
DTC	Direct Torque Control
PTC	Predictive Torque Control
MPC	Model Predictive Control
CCS-MPC	Continuous Control Set Model Predictive Control
FCS-MPC	Finite Control Set Model Predictive Control
PI	Proportional Integral
HIL	Hardware in the Loop
PWM	Pulse Width Modulation
SPWM	Sinusoidal Pulse Width Modulation
SVM	Space Vector Modulation
IAE	Integral of the Absolute Error
RMSE	Root Mean Squared Error
RRMSE	Relative Root Mean Squared Error
THD	Total Harmonic Distortion
SOC	State of Charge

References

1. Thangavel, S.; Mohanraj, D.; Girijaprasanna, T.; Raju, S.; Dhanamjayulu, C.; Muyeen, S.M. A Comprehensive Review on Electric Vehicle: Battery Management System, Charging Station, Traction Motors. *IEEE Access* **2023**, *11*, 20994–21019. [\[CrossRef\]](#)
2. Zhang, X.; Lu, Z.; Yuan, X.; Wang, Y.; Shen, X. L2-Gain Adaptive Robust Control for Hybrid Energy Storage System in Electric Vehicles. *IEEE Trans. Power Electron.* **2021**, *36*, 7319–7332. [\[CrossRef\]](#)
3. Zhang, L.; Yin, Q.; Zhu, W.; Lyu, L.; Jiang, L.; Koh, L.H.; Cai, G. Research on the orderly charging and discharging mechanism of electric vehicles considering travel characteristics and carbon quota. *IEEE Trans. Transp. Electrif.* **2023**. [\[CrossRef\]](#)
4. Zhang, L.; Sun, C.; Cai, G.; Koh, L.H. Charging and discharging optimization strategy for electric vehicles considering elasticity demand response. *eTransportation* **2023**, *18*, 100262. [\[CrossRef\]](#)
5. Min, H.; Fang, Y.; Wu, X.; Lei, X.; Chen, S.; Teixeira, R.; Zhu, B.; Zhao, X.; Xu, Z. A fault diagnosis framework for autonomous vehicles with sensor self-diagnosis. *Expert Syst. Appl.* **2023**, *224*, 120002. [\[CrossRef\]](#)
6. Min, C.; Pan, Y.; Dai, W.; Kawsar, I.; Li, Z.; Wang, G. Trajectory optimization of an electric vehicle with minimum energy consumption using inverse dynamics model and servo constraints. *Mech. Mach. Theory* **2023**, *181*, 105185. [\[CrossRef\]](#)
7. Ding, C.; Li, C.; Xiong, Z.; Li, Z.; Liang, Q. Intelligent Identification of Moving Trajectory of Autonomous Vehicle Based on Friction Nano-Generator. *IEEE Trans. Intell. Transp. Syst.* **2023**. [\[CrossRef\]](#)

8. Almeida, A.T.D.; Ferreira, F.J.; Fong, J.A.; Brunner, C.U. Electric motor standards, ecodesign and global market transformation. In Proceedings of the 2008 IEEE/IAS Industrial and Commercial Power Systems Technical Conference, Sydney, NSW, Australia, 4–8 May 2008. [[CrossRef](#)]
9. Xue, X.D.; Cheng, K.W.; Cheung, N.C. Selection of electric motor drives for electric vehicles. In Proceedings of the 2008 Australasian Universities Power Engineering Conference, Sydney, NSW, Australia, 14–17 December 2008.
10. Pellegrino, G.; Vagati, A.; Boazzo, B.; Guglielmi, P. Comparison of induction and PM synchronous motor drives for EV application including design examples. *IEEE Trans. Ind. Appl.* **2012**, *48*, 2322–2332. [[CrossRef](#)]
11. Yang, Z.; Shang, F.; Brown, I.P.; Krishnamurthy, M. Comparative study of interior permanent magnet, induction, and switched reluctance motor drives for EV and HEV applications. *IEEE Trans. Transp. Electr.* **2015**, *1*, 245–254. [[CrossRef](#)]
12. Santiago, J.D.; Bernhoff, H.; Ekergård, B.; Eriksson, S.; Ferhatovic, S.; Waters, R.; Leijon, M. Electrical motor drivelines in commercial all-electric vehicles: A review. *IEEE Trans. Veh. Technol.* **2012**, *61*, 475–484. [[CrossRef](#)]
13. Rind, S.J.; Jamil, M.; Amjad, A. Electric Motors and Speed Sensorless Control for Electric and Hybrid Electric Vehicles: A Review. In Proceedings of the 2018 53rd International Universities Power Engineering Conference, Glasgow, UK, 4–7 September 2018. [[CrossRef](#)]
14. Muñoz-García, A.; Lipo, T.A.; Novotny, D.W. A New induction motor v/f control method capable of high-performance regulation at low speeds. *IEEE Trans. Ind. Appl.* **1998**, *34*, 813–821. [[CrossRef](#)]
15. Lee, J.W. Novel Current Control Assisted V/F Control Method for High Speed Induction Motor Drives. In Proceedings of the 10th International Conference on Power Electronics-ECCE Asia, Busan, Republic of Korea, 27–30 May 2019; pp. 1293–1296. [[CrossRef](#)]
16. Boldea, I. Control issues in adjustable speed drives. *IEEE Ind. Electron. Mag.* **2008**, *2*, 32–50. [[CrossRef](#)]
17. Bobin, V.J.; Beno, M.M. Performance Analysis of Optimization Based FOC and DTC Methods for Three Phase Induction Motor. *Intell. Autom. Soft Comput.* **2023**, *35*, 2493–2511. [[CrossRef](#)]
18. Saady, I.; Karim, M.; Bossoufi, B.; Motahhir, S.; Adouairi, M.S.; Majout, B.; Lamnadi, M.; Masud, M.; Al-Amri, J.F. Optimization for a Photovoltaic Pumping System Using Indirect Field Oriented Control of Induction Motor. *Electronics* **2021**, *10*, 3076. [[CrossRef](#)]
19. Rodríguez, J.; Kennel, R.M.; Espinoza, J.R.; Trincado, M.; Silva, C.A.; Rojas, C.A. High-performance control strategies for electrical drives: An experimental assessment. *IEEE Trans. Ind. Electron.* **2012**, *59*, 812–820. [[CrossRef](#)]
20. Barut, M.; Bogosyan, S.; Gokasan, M. Speed-sensorless estimation for induction motors using extended Kalman filters. *IEEE Trans. Ind. Electron.* **2007**, *54*, 272–280. [[CrossRef](#)]
21. Buja, G.S.; Kazmierkowski, M.P. Direct torque control of PWM inverter-fed AC motors—A survey. *IEEE Trans. Ind. Electron.* **2004**, *51*, 744–757. [[CrossRef](#)]
22. Casadei, D.; Profumo, F.; Serra, G.; Tani, A. FOC and DTC: Two viable schemes for induction motors torque control. *IEEE Trans. Power Electron.* **2002**, *17*, 779–787. [[CrossRef](#)]
23. Perez-Guzman, R.E.; Rivera, M.; Wheeler, P.W. Predictive Control Strategies in Power Converters. In Proceedings of the IEEE CHILEAN Conference on Electrical, Electronics Engineering, Information and Communication Technologies, CHILECON 2019, Valparaiso, Chile, 13–27 November 2019. [[CrossRef](#)]
24. Ahmed, A.A.; Koh, B.K.; Lee, Y.I. A Comparison of Finite Control Set and Continuous Control Set Model Predictive Control Schemes for Speed Control of Induction Motors. *IEEE Trans. Ind. Informatics* **2018**, *14*, 1334–1346. [[CrossRef](#)]
25. Lim, C.S.; Levi, E.; Jones, M.; Rahim, N.A.; Hew, W.P. FCS-MPC-based current control of a five-phase induction motor and its comparison with PI-PWM control. *IEEE Trans. Ind. Electron.* **2014**, *61*, 149–163. [[CrossRef](#)]
26. Diab, A.A.Z.; Kotin, D.A.; Anosov, V.N.; Pankratov, V.V. A comparative study of speed control based on MPC and PI-controller for Indirect Field oriented control of induction motor drive. In Proceedings of the 2014 12th International Conference on Actual Problems of Electronic Instrument Engineering, APEIE 2014-Proceedings, Novosibirsk, Russia, 2–4 October 2014; pp. 728–732. [[CrossRef](#)]
27. Huang, J.; Jiang, G.; Zhang, P.; Chen, J. A Low Switching Frequency Model Predictive Control Method for an Induction Motor Fed by a 3-Level Inverter. *Electronics* **2023**, *12*, 3609. [[CrossRef](#)]
28. Cataldo, P.; Jara, W.; Riedemann, J.; Pesce, C.; Andrade, I.; Pena, R. A Predictive Current Control Strategy for a Medium-Voltage Open-End Winding Machine Drive. *Electronics* **2023**, *12*, 1070. [[CrossRef](#)]
29. Wang, H.; Wu, X.; Zheng, X.; Yuan, X. Model Predictive Current Control of Nine-Phase Open-End Winding PMSMs With an Online Virtual Vector Synthesis Strategy. *IEEE Trans. Ind. Electron.* **2023**, *70*, 2199–2208. [[CrossRef](#)]
30. Myaing, A.; Dinavahi, V. FPGA-based real-time emulation of power electronic systems with detailed representation of device characteristics. *IEEE Trans. Ind. Electron.* **2011**, *58*, 358–368. [[CrossRef](#)]
31. Saleem, A.; Issa, R.; Tutunji, T. Hardware-In-the-Loop for on-line identification and control of three-phase squirrel cage induction motors. *Simul. Model. Pract. Theory* **2010**, *18*, 277–290. [[CrossRef](#)]
32. Bose, B.K. *Power Electronics and Motor Drives: Advances and Trends*; Academic Press: Cambridge, MA, USA, 2006; pp. 1–917. [[CrossRef](#)]
33. Vetter, M.; Lux, S. Rechargeable Batteries with Special Reference to Lithium-Ion Batteries. In *Storing Energy: With Special Reference to Renewable Energy Sources*; Elsevier: Amsterdam, The Netherlands, 2016; pp. 205–225. [[CrossRef](#)]
34. Aaldering, L.J.; Song, C.H. Tracing the technological development trajectory in post-lithium-ion battery technologies: A patent-based approach. *J. Clean. Prod.* **2019**, *241*, 118343. [[CrossRef](#)]

35. Diouf, B.; Pode, R. Potential of lithium-ion batteries in renewable energy. *Renew. Energy* **2015**, *76*, 375–380. [[CrossRef](#)]
36. Hu, J.; Karava, P. A state-space modeling approach and multi-level optimization algorithm for predictive control of multi-zone buildings with mixed-mode cooling. *Build. Environ.* **2014**, *80*, 259–273. [[CrossRef](#)]
37. Islam, M.; Okasha, M. A Comparative Study of PD, LQR and MPC on Quadrotor Using Quaternion Approach. In Proceedings of the 2019 7th International Conference on Mechatronics Engineering, ICOM 2019, Putrajaya, Malaysia, 30–31 October 2019. [[CrossRef](#)]
38. Kim, S.H. *Electric Motor Control*; Elsevier: Amsterdam, The Netherlands, 2017; pp. i–iii.
39. Alkorta, P.; Barambones, O.; Zubizarreta, A.; Cortajarena, J.A. Effective and robust generalized predictive speed control of induction motor. *Math. Probl. Eng.* **2013**, 2013. [[CrossRef](#)]
40. Kostopoulos, E.D.; Spyropoulos, G.C.; Kaldellis, J.K. Real-world study for the optimal charging of electric vehicles. *Energy Rep.* **2020**, *6*, 418–426. [[CrossRef](#)]
41. Abdelaal, A.S.; Mukhopadhyay, S.; Rehman, H. Battery Energy Management Techniques for an Electric Vehicle Traction System. *IEEE Access* **2022**, *10*, 84015–84037. [[CrossRef](#)]

Disclaimer/Publisher’s Note: The statements, opinions and data contained in all publications are solely those of the individual author(s) and contributor(s) and not of MDPI and/or the editor(s). MDPI and/or the editor(s) disclaim responsibility for any injury to people or property resulting from any ideas, methods, instructions or products referred to in the content.